Characterizing genetic intra-tumor heterogeneity across 2,658 human cancer genomes

Stefan C. Dentro[1,2,3,#], Ignaty Leshchiner[4,#], Kerstin Haase[1,#], Maxime Tarabichi[1,2,#], Jeff Wintersinger[5,#], Amit G. Deshwar[5,#], Kaixian Yu[6,#], Yulia Rubanova[5,#], Geoff Macintyre[7,#], Jonas Demeulemeester[1,8,#], Ignacio Vázquez-García[2,9,10,11], Kortine Kleinheinz[12,13], Dimitri G. Livitz[4], Salem Malikic[14], Nilgun Donmez[14], Subhajit Sengupta[15], Pavana Anur[16], Clemency Jolly[1], Marek Cmero[17], Daniel Rosebrock[4], Steven Schumacher[4], Yu Fan[6], Matthew Fittall[1], Ruben M. Drews[7], Xiaotong Yao[18,19], Juhee Lee[20], Matthias Schlesner[10], Hongtu Zhu[6], David J. Adams[2], Gad Getz[4], Paul C. Boutros[5,21], Marcin Imielinski[18,19], Rameen Beroukhim[4], S. Cenk Sahinalp[22], Yuan Ji[15,23], Martin Peifer[24], Inigo Martincorena[2], Florian Markowetz[7], Ville Mustonen[25], Ke Yuan[7,26], Moritz Gerstung[27], Paul T. Spellman[16], Wenyi Wang[6,#], Quaid D. Morris[5,#], David C. Wedge[3,28,#], Peter Van Loo[1,#,*], on behalf of the PCAWG Evolution and Heterogeneity Working Group[29] and the PCAWG consortium.

[1]The Francis Crick Institute, London, United Kingdom; [2]Wellcome Trust Sanger Institute, Cambridge, United Kingdom; [3]Big Data Institute, University of Oxford, Oxford, United Kingdom; [4]Broad Institute of MIT and Harvard, Cambridge, MA, USA; [5]University of Toronto, Toronto, Canada; [6]The University of Texas MD Anderson Cancer Center, Houston, TX, USA; [7]Cancer Research UK Cambridge Institute, University of Cambridge, Cambridge, United Kingdom; [8]Department of Human Genetics, University of Leuven, Leuven, Belgium; [9]University of Cambridge, Cambridge, United Kingdom; [10]Computational Oncology, Memorial Sloan Kettering Cancer Center, New York, NY, USA; [11]Irving Institute for Cancer Dynamics, Columbia University, New York, NY, USA; [12]German Cancer Research Center (DKFZ), Heidelberg, Germany; [13]Heidelberg University, Heidelberg, Germany; [14]Simon Fraser University, Vancouver, Canada; [15]NorthShore University HealthSystem, Evanston, IL, USA; [16]Molecular and Medical

29 Genetics, Oregon Health & Science University, Portland, OR, USA; [17]University of
30 Melbourne, Melbourne, Australia; [18]Weill Cornell Medicine, New York, NY, USA; [19]New
31 York Genome Center, New York, NY, USA; [20]University of California Santa Cruz, Santa
32 Cruz, CA, USA; [21]University of California, Los Angeles, Los Angeles, CA, USA; [22]Indiana
33 University, Bloomington, IN, USA; [23]The University of Chicago, Chicago, IL, USA;
34 [24]University of Cologne, Cologne, Germany; [25]Organismal and Evolutionary Biology
35 Research Programme, Department of Computer Science, Institute of Biotechnology,
36 University of Helsinki, Helsinki, Finland; [26]School of Computing Science, University of
37 Glasgow, Glasgow, United Kingdom; [27]European Molecular Biology Laboratory,
38 European Bioinformatics Institute, Cambridge, United Kingdom; [28]Oxford NIHR
39 Biomedical Research Centre, Oxford, United Kingdom.

40

41 [#]These authors contributed equally.

42

43 [*]To whom correspondence may be addressed:

44 Peter Van Loo, The Francis Crick Institute, 1 Midland Road, London, NW1 1AT, United
45 Kingdom. Tel: +44 (0) 20 3796 1719, e-mail: Peter.VanLoo@crick.ac.uk.

46

47 [29]A list of members of the PCAWG Evolution and Heterogeneity Working Group can be
48 found at the end of the manuscript.

SUMMARY

Intra-tumor heterogeneity (ITH) is a mechanism of therapeutic resistance and therefore an important clinical challenge. However, the extent, origin and drivers of ITH across cancer types are poorly understood. To address this question, we extensively characterize ITH across whole-genome sequences of 2,658 cancer samples, spanning 38 cancer types. Nearly all informative samples (95.1%) contain evidence of distinct subclonal expansions, with frequent branching relationships between subclones. We observe positive selection of subclonal driver mutations across most cancer types, and identify cancer type specific subclonal patterns of driver gene mutations, fusions, structural variants and copy-number alterations, as well as dynamic changes in mutational processes between subclonal expansions. Our results underline the importance of ITH and its drivers in tumor evolution, and provide an unprecedented pan-cancer resource of comprehensively annotated subclonal events from whole-genome sequencing data.

62 **INTRODUCTION**

63 Cancers accumulate somatic mutations as they evolve (Nowell, 1976; Tabin et al., 1982).
64 Some of these mutations are drivers that confer fitness advantages to their host cells and
65 can lead to clonal expansions (Garraway and Lander, 2013; Greaves and Maley, 2012;
66 Stratton et al., 2009; Vogelstein et al., 2013). Late clonal expansions, spatial segregation,
67 and incomplete selective sweeps result in genetically distinct cellular populations that
68 manifest as intra-tumor heterogeneity (ITH) (Nowell, 1976). Clonal mutations are shared
69 by all cancer cells, whereas subclonal mutations are present only in a fraction of cancer
70 cells.

71 ITH represents an important clinical challenge, as it provides genetic variation that may
72 drive cancer progression and lead to the emergence of drug resistance (Maley et al., 2006;
73 McGranahan and Swanton, 2017; Mroz et al., 2013). Subclonal drug resistance and
74 associated driver mutations are common (Gerlinger et al., 2012; Gundem et al., 2015;
75 Landau et al., 2013; McGranahan et al., 2015; Shaw et al., 2016; Yates et al., 2015). ITH
76 can impact clinical trial design (Hiley et al., 2014), predict progression (Maley et al., 2004),
77 and can be directly prognostic (Espiritu et al., 2018). For example, ITH at the level of copy
78 number aberrations (CNAs) is associated with increased risk of relapse in non-small cell
79 lung cancer (Jamal-Hanjani et al., 2017), head and neck cancer (Mroz and Rocco, 2013;
80 Rocco, 2015) and glioblastoma multiforme (Brastianos et al., 2017).

81 ITH can be characterized from massively parallel sequencing data (Campbell et al., 2008;
82 Landau et al., 2013; McGranahan et al., 2015; Nik-Zainal et al., 2012; Sottoriva et al.,
83 2013), as the cells comprising a clonal expansion share a unique set of driver and passenger
84 mutations derived from the expansion-initiating cell. Each mutation within this shared set
85 is present in the same proportion of tumor cells (known as cancer cell fraction, CCF), which
86 may be estimated by adjusting mutation allele frequencies for local copy number and
87 sample purity. Subsequent clustering of mutations based on their CCF yields the 'subclonal
88 architecture' of a sample (Dentro et al., 2017): estimates of the number of tumor cell
89 populations in the sequenced sample, the CCF of each population, and assignments of
90 mutations to each population.

91 To date, ITH remains poorly characterized across cancer types, and there is substantial
92 uncertainty concerning the selective pressures operating on subclonal populations.
93 Previous pan-cancer efforts used the principles above to characterize subclonal events, but
94 have been limited to exomes, which restricts the number and resolution of somatic mutation
95 calls and ignores structural variation (Andor et al., 2016). Two recent studies using pan-
96 cancer data from The Cancer Genome Atlas found that actionable driver mutations are
97 often subclonal (McGranahan et al., 2015), and that ITH has broad prognostic value (Andor
98 et al., 2016).

99 Recent studies have relied on multi-region whole-genome, exome or targeted sequencing
100 to characterize ITH in detail in specific cancer types (Jamal-Hanjani et al., 2017;
101 McPherson et al., 2016; Turajlic et al., 2018b; Yates et al., 2015). Due to the 'illusion of
102 clonality' (de Bruin et al., 2014), variants found as clonal in one sample may be subclonal
103 in other samples from the same tumor, and therefore single-sample analyses can
104 underestimate the extent of ITH. The converse is also true: any mutations detected as
105 subclonal in any single sample, will by definition be subclonal no matter how many
106 samples have been assayed. Therefore, through analyzing single cancer samples, a
107 conservative lower limit of ITH can be established.

108 Here, we develop a robust consensus strategy that maintains conservative inferences to call
109 copy number and cluster mutations in order to assess ITH, its origin, its drivers, and its role
110 in tumor development. We apply these approaches to 2,658 tumors from 38 histologically
111 distinct cancer types from the Pan-Cancer Analysis of Whole Genomes (PCAWG)
112 initiative (The ICGC/TCGA Pan-Cancer Analysis of Whole Genomes Consortium, 2020).
113 In comparison to exome sequencing, whole-genome sequencing data provides orders of
114 magnitude more point mutations, greater resolution to detect CNAs and the ability to call
115 structural variants (SVs). Collectively, these substantially increase the breadth and depth
116 of our ITH analyses permitting us to find pervasive ITH across all cancer types. We are
117 further able to observe frequent branching patterns of subclonal evolution and clear signs
118 of positive selection in subclones. We identify subclonal driver mutations in known cancer
119 genes and unanticipated changes in mutation signature activity across many cancer types.
120 In total, these analyses provide detailed insight into tumor evolutionary dynamics.

121 # RESULTS

122 **Consensus-based characterization of intra-tumor heterogeneity in 2,658 cancers**

123 We set out to characterize ITH across cancer types, including single-nucleotide variants
124 (SNVs), indels, SVs and CNAs, as well as subclonal drivers, subclonal selection, and
125 mutation signatures. We leveraged the PCAWG dataset, encompassing 2,778 whole-
126 genome sequences from 2,658 human tumors across 38 distinct histological cancer types
127 (Alexandrov et al., 2020; Gerstung et al., 2020; Rheinbay et al., 2020; The ICGC/TCGA
128 Pan-Cancer Analysis of Whole Genomes Consortium, 2020).

129 First, to generate high-confidence calls, we developed ensemble approaches for variant
130 calling, copy number calling and subclonal reconstruction (**Figure 1A**, **STAR Methods**).
131 Specifically, to maximize sensitivity and specificity of calling clonal and subclonal
132 mutations, the PCAWG consortium developed and extensively validated a robust
133 consensus approach integrating the output of four SNV calling algorithms (The
134 ICGC/TCGA Pan-Cancer Analysis of Whole Genomes Consortium, 2020). Similar
135 consensus approaches were employed for indels and SVs.

136 As previous studies report that the quality of copy number calls has a large effect on the
137 robustness of subclonal reconstruction (Andor et al., 2016; Salcedo et al., 2020), we
138 devised a systematic approach to consensus copy number calling, integrating results from
139 six state-of-the-art copy number callers (**Figure 1A**, **STAR Methods**). Each algorithm was
140 run twice, first to identify all copy number breakpoints and construct a consensus
141 segmentation. To improve sensitivity and obtain breakpoints at base-pair resolution, SV
142 breakpoints were also inserted into these first runs (**STAR Methods**). In a second run, this
143 consensus segmentation was enforced on all CNA callers, resulting in copy number calls
144 with identical breakpoints across algorithms.

145 Purity and ploidy assessment of cancer samples can be challenging, as for some samples
146 multiple purity/ploidy combinations can be theoretically possible and these may be difficult
147 to distinguish (Carter et al., 2012; Van Loo et al., 2010). Consensus purity and ploidy were
148 determined by establishing agreement between the six CNA callers (**STAR Methods**). An
149 expert panel reviewed and resolved cases where the callers disagreed. We found that the

150 purity values correlate strongly with a recent cross-omics analysis of tumor purity (Aran et
151 al., 2015) (**Figure S1**). After establishing agreement on the purity and ploidy, we defined
152 samples that had undergone whole-genome duplication in an objective and automated way,
153 based on tumor ploidy and the extent of loss of heterozygosity (**Figure 1B**, **STAR**
154 **Methods**). This classification shows 98.7% agreement with an alternative approach
155 leveraging the mode of the major allele (Carter et al., 2012). However, our classification
156 correctly classifies difficult tumors with many large chromosome gains, such as
157 medulloblastomas or pancreatic endocrine tumors, whereas the alternative approach is less
158 suitable for these tumors and occasionally makes errors. In addition, samples with whole-
159 genome duplications showed synchronous chromosomal gains (Gerstung et al., 2020),
160 further validating our approach. To further support high-quality subclonal reconstruction,
161 the whole genome of each tumor was annotated for the confidence in the consensus copy
162 number calls, which were assigned 'tiers' based on the level of agreement between different
163 callers. On average, we reached a high confidence consensus on 93% of the genome
164 (median: 95%, standard deviation: 13%) (**Figure 1C**, **STAR Methods**).

165 Consensus copy number profiles, SNVs, and purity estimates served as input to 11
166 subclonal architecture reconstructing methods, and the results of these methods were
167 combined into a single consensus reconstruction for each tumor (**Figure 1A**, **STAR**
168 **Methods**). Due to the probabilistic nature of subclonal reconstruction, we developed three
169 consensus approaches using different summary outputs of individual methods. We
170 validated the results of the consensus strategies on two independently simulated datasets
171 and assessed their robustness on the real data. The consensus methods performed
172 comparably to the best individual methods on both simulated datasets, with the top-
173 performing individual methods also displaying high similarity scores (**Figure 1D**, **STAR**
174 **Methods**). Whereas true mutations and CNAs were used in the analysis of simulated data,
175 in the real data the true subclonal mutations and CNAs are unknown. On the real data, the
176 highest similarities were observed for the consensus approaches, and not among individual
177 methods (**Figure 1D**), confirming that our consensus approaches yield the most robust
178 subclonal reconstruction outcome. Furthermore, using one simulated dataset with 965
179 samples, we evaluated the performances of our consensus methods over all 2,035 possible

180 combinations of 11 individual methods. We observed that the most robust performance,
181 when the best callers are not known *a priori*, was achieved when all 11 callers were
182 combined (**STAR Methods**). Hence, we used the output of one of our consensus methods,
183 combining all 11 individual callers, as the basis for our global assignment strategy (**STAR**
184 **Methods**). Through this approach, we obtained the number of detectable subclonal
185 expansions, the fraction of subclonal SNVs, indels, SVs and CNAs, as well as the
186 assignment of SNVs, indels and SVs to subclones for each tumor.

187 To obtain unbiased estimates of the number of mutations in the detected subclones and
188 their CCFs, we accounted for a detection bias introduced by somatic variant calling.
189 Specifically, as the CCF of a subclone decreases, so does the power to detect the SNVs
190 associated with that subclone. This leads to biases in the estimates of subclone parameters,
191 such as an overestimation of the subclone's CCF, akin to the "winner's curse" (Nik-Zainal
192 et al., 2012). In addition, an increasing number of uncalled SNVs in the subclone leads to
193 an underestimation of the number of associated mutations. The larger number of SNVs
194 revealed by WGS (compared to whole-exome sequencing) facilitates quantitation and
195 correction of these biases. We developed two methods to do this, validated them on
196 simulated data (**STAR Methods**, **Figure 2A**), and combined them to correct the estimated
197 number of SNVs and the CCF of each subclone. We estimate that, on average, 14% of
198 SNVs in detectable subclones are below the somatic caller detection limits (**Figures 2B-**
199 **C**). In particular, in subclones with CCF < 30%, on average 21% of SNVs are missed. Due
200 to the complexity in modelling sensitivity of indel and SV calling as a function of the
201 number of variant reads, similar models could not be developed for these mutation types.
202 However, we anticipate that higher fractions of SVs and indels are likely missed because
203 of the lower sensitivity of existing algorithms (The ICGC/TCGA Pan-Cancer Analysis of
204 Whole Genomes Consortium, 2020). In addition, these values only include SNVs missed
205 in detected subclones, not SNVs in subclones that remain undetected due to limited
206 sequencing depth.

207

208

209 **Pervasive intra-tumor heterogeneity across cancer types**

210 We first evaluated the number of subclones identified by our consensus approach. We
211 noted a strong correlation between the average effective read depth along the genome
212 (sequencing coverage per haploid genome copy, i.e. the amount of sequencing signal) and
213 the number of identified subclones (**Figure S2**), and therefore focused on 1,705 cancer
214 genomes where our approach is powered to detect subclones encompassing >30% of tumor
215 cells (**STAR Methods**). One or more subclonal expansions were evident in 1,621 tumors
216 (95.1%), while only 84 tumors (4.9%) were clonal at the resolution of our methods (**Figure**
217 **3A**). Importantly, these estimates, based on single-sample reconstruction and a median
218 ~46X read coverage, provide only a conservative lower bound for the number of subclones,
219 as this study is not powered to detect rare subclonal populations.

220 Looking across cancer types (**Figure 3A**), our consensus approach finds a high proportion
221 of samples with at least one subclone (>75%) in all cancer types, except cutaneous
222 melanoma, where subclones were detectable by our approach in only half of the samples
223 (31/62). In contrast, acral melanomas followed the pattern observed in other cancer types
224 with higher frequencies of subclonal expansions (14/16 samples, 87.5%). Twenty-five out
225 of 30 cancer types with more than 10 cases comprised >90% of samples with at least one
226 detectable subclone, indicating pervasive ITH across cancer types.

227 The fraction of subclonal SNVs identified after winner's curse correction varies widely
228 across cancer types (**Figure 3B**). Squamous cell carcinomas typically show low fractions
229 of subclonal SNVs (head-and-neck, 9.7% ± 11.9; lung, 6.1% ± 6.7; cervix, 20.6% ± 19.6;
230 mean ± standard deviation), while prostate adenocarcinoma (41.2% ± 21.8), thyroid
231 adenocarcinoma (42.8% ± 19.6), chromophobe renal cell carcinomas (45.2% ± 22.7),
232 pancreatic neuroendocrine tumors (46% ± 24.7) and pilocytic astrocytomas (61.3% ± 14.8)
233 showed the highest fractions of subclonal SNVs.

234 Indels, SVs and CNAs also revealed similarly large differences between cancer types. For
235 indels, the subclonal fraction ranged from 6.2% ± 11.7 in lung squamous carcinomas to
236 43.4% ± 23.7 in pancreatic neuroendocrine tumors (**Figure 3C**). For SVs, liposarcomas
237 and cutaneous melanomas showed the lowest subclonal fraction (8.0% ± 14.1 and 8.9% ±

238 15.5 respectively) and chromophobe renal cell cancers the highest (56.8% ± 31.6) (**Figure**
239 **3D**). The fraction of subclonal copy number changes was lowest in chromophobe renal cell
240 cancers (13.3% ± 16.8) and highest in prostate adenocarcinoma (53.8% ± 32.0) (**Figure**
241 **3E**). Comparing these values to the SNV burden (**Figure 3F**), the fraction of the genome
242 affected by CNAs (**Figure 3G**), the frequency of WGD per cancer type (**Figure 3H**), and
243 the power to identify subclones per cancer type (**Figure 3I**) showed that none of these
244 metrics explain this wide variation. While we observed that cancer types with higher
245 mutation burden showed lower fractions of subclonal SNVs (**Figures 3B and 3F**), we did
246 not see a similar relationship when evaluating individual tumors (**STAR Methods**). The
247 proportions of subclonal indels and SNVs are strongly correlated (R^2 = 0.73). SVs follow
248 a similar trend (R^2 = 0.62 with indels, R^2 = 0.51 with SNVs), except for liver, colorectal
249 and ovarian tumors, which show higher fractions of subclonal SVs than SNVs (**Figures**
250 **3B-E and S3**). In contrast, the average proportions of subclonal large-scale CNAs and
251 SNVs are only weakly correlated (R^2 = 0.24), indicating these could be driven by
252 independent mutational processes.

253 Some cancer types had limited ITH across all mutation types (e.g. biliary cancers,
254 squamous cell carcinomas and stomach cancers), while other cancer types showed an
255 abundance of ITH in specific somatic variant categories. For example, chromophobe
256 kidney cancers and pancreatic neuroendocrine tumors have few subclonal CNAs but a high
257 subclonal burden across all other variant categories (**Figures 3B-E**). Finally, among the
258 tumors of each cancer type, we find substantial diversity in the fraction of subclonal
259 variants (**Figures 3B-E**).

260 These findings highlight the high prevalence of ITH across cancer types. Nearly all tumors
261 assayed here, irrespective of cancer type, show evidence of subclonal expansions giving
262 rise to detectable subclonal populations, even at a limited read depth. In addition, we find
263 that the average proportions of subclonal SNVs, indels, SVs and CNAs are highly variable
264 across cancer types. These analyses paint characteristic portraits of the nature of ITH,
265 suggesting distinct evolutionary narratives for each histological cancer type.

266

267 **Complex phylogenies among subclones revealed by whole genome sequencing**

268 Whole-genome sequencing provides an opportunity to explore and reconstruct additional
269 patterns of subclonal structure by performing phasing of pairs of mutations in the same
270 read pair, to assess evolutionary relationships of subclonal lineages (**Figures 4A-B**). Two
271 subclones can be either linearly related to each other (parent-child relationship), or have a
272 common ancestor, but develop on branching lineages (sibling subclones). Establishing
273 evolutionary relationships between subclones is challenging on single-sample sequencing
274 data due to the limited resolution to separate subclones and the uncertainties on their CCF
275 estimates. We can, however, examine pairs of SNVs in WGS data that are covered by the
276 same read pairs (*i.e.* phaseable SNV pairs), to reconstruct this relationship. Specifically,
277 evidence for a parent-child relationship between two clones is given by a SNV pattern in a
278 region without copy number gains, where the SNV attributed to the child clone is only
279 found on a subset of the reads that carry the SNV attributed to the parent clone (**Figure 4A**,
280 **STAR Methods**). Similarly, evidence for a sibling relationship between two clones is
281 given by an SNV pattern in a haploid region where overlapping read pairs carry either the
282 SNV attributed to one clone or the other (but not both) (**Figure 4B**, **STAR methods**). As
283 the number of read pairs carrying two variants depends strongly on mutation burden and
284 specific copy number context, they are generally extremely rare. Our large, curated dataset,
285 however, enables us to identify a sizeable total of these and explore their phylogenetic
286 information content in detail.

287 We find that of 1,537 tumors with sufficient power and at least one phaseable pair in the
288 correct context, 245 show discordant in-*cis* SNVs pairs, indicating parent-child
289 relationships (**Figure 4A**). Annotating SNVs with their clone or subclone assignment from
290 CCF clustering, the vast majority of these samples (233, 95.1%) show pairs supporting the
291 expected clone-subclone relationship. In addition, there are 8 samples with pairs assigned
292 to different subclones and 16 samples with pairs assigned to the same subclone,
293 highlighting collinear evolution among subclones. Of 995 tumors, 51 carry discordant in-
294 *trans* SNVs pairs, with 32 and 27 of these samples having pairs assigned to the same or
295 different subclones, respectively (8 have both), confirming the occurrence of two sibling
296 subclones having expanded in parallel (**Figure 4B**).

297 The identification of subclones from phaseable SNV pairs can be considered largely
298 independent of the consensus subclonal reconstruction. One can therefore use phasing
299 results to assess the performance of subclonal reconstruction and *vice versa*. Indeed, tumors
300 identified to contain higher numbers of subclones according to the consensus
301 reconstruction are enriched for linear and branching pairs (p-value = 3.9×10^{-15}, **Figure 4C**).
302 Nevertheless, our identification of 16 and 32 samples with SNV pairs assigned to the same
303 subclone but showing in-*cis* and in-*trans* discordance, respectively, confirms that our
304 consensus approach identifies only a lower limit on the number of subclonal expansions.
305 Interestingly, 8 of the 13 cutaneous melanomas showing linear or branching pairs had been
306 deemed clonal by CCF clustering but had phasing evidence for 1–2 subclones (3 had linear,
307 7 had branching, and 3 had both linear and branching SNV pairs). This analysis suggests
308 that, similarly to other cancer types, the large majority of cutaneous melanomas contain
309 subclonal expansions. However, these might be obscured by the large numbers of clonal
310 mutations in these extremely highly mutated tumors.

311 The frequency of branching versus linear evolution can be assessed directly by subsetting
312 the phasing analysis to haploid regions and to pairs where both SNVs have been assigned
313 to subclones, as both linear and branching relationships may be detected with similar power
314 in this subset. Our results indicate that, in the pan-cancer setting, two subclones are 3.11
315 times more likely to be siblings than to have a parent-child relationship (bootstrapped 95%
316 confidence interval [1.71; 7.50], **Figure 4D**). This result is consistent with the complex
317 phylogenies obtained from multi-region sequencing efforts such as the TRACERx 100
318 non-small-cell lung cancer cohort (Jamal-Hanjani et al., 2017), where the odds of
319 branching *vs.* linear evolution are 2.86 (bootstrapped 95% confidence interval [1.93; 5.07],
320 **Figure 4E**, **STAR Methods)**. These results are also in line with observations of mutual
321 exclusivity of subclonal drivers and extensive parallel evolution (Turajlic et al., 2018a;
322 Turajlic et al., 2018b).

323

324 **Patterns of subclonal mutation signature activity changes across cancers**

325 Mutation processes can differ in their activity between clonal and subclonal lineages

326 (McGranahan et al., 2015). To explore the subclonal dynamics of mutation signatures in
327 detail, we examined subclonal mutations for changes in signature activity. We reasoned
328 that if a mutation process is activated during a specific subclonal expansion, only the post-
329 expansion mutations will carry the corresponding mutation signature. Signature activity
330 change points can therefore be identified in SNVs that are rank-ordered by their CCFs
331 estimates (Rubanova et al., 2020) (**STAR Methods**). Of the 2,552 samples with sufficient
332 SNVs to perform this analysis, 1,944 (76%) have an activity change of at least 5% in at
333 least one signature (a conservative threshold established *via* permutation and bootstrapping
334 analyses, **STAR Methods**). We detect an average of 1.77 mutation signature activity
335 clusters per sample.

336 Overall, mutation signature activity is remarkably stable. The most frequently changing
337 signature (Signature SBS12, etiology unknown (Alexandrov et al., 2020), active in 198 of
338 326 (61%) liver cancers), is variable in approximately 60% of the cases in which it is active
339 (**Figure 5A**). In addition, we find that the activity of Signature SBS9 (Pol η activity on
340 AID lesions) decreases as a function of decreasing CCF in over half the tumors in which
341 this signature is active (CLL and B-cell non-Hodgkin lymphoma). When only considering
342 pairs of signatures that change in the same tumor, we see that 6 out of the top 10 pairs
343 involve SBS5 (etiology unknown but hypothesized to reflect lower-fidelity DNA repair
344 pathways (Kim et al., 2016)). Such changes in proportions are often anti-correlated, as the
345 activity of one mutation process may be changing at the proportional expense of the activity
346 of another.

347 We next evaluated signature trajectories per cancer type (**Figure 5A**). In CLL, SBS9
348 always decreases and SBS5 nearly always increases. In contrast, in ovarian cancers, most
349 signature activity changes go both up and down in similar, relatively low proportions of
350 tumors. On average, signature activity changes are modest in size, with the maximum
351 average activity change recorded in CLL (33%, SBS9). Some changes are observed across
352 many cancer types - *e.g.*, SBS5 and SBS40, of unknown etiology - while others are found
353 in only one or a few cancer types. For example, in hepatocellular carcinomas, we observe
354 an increase in SBS35 and a decrease in SBS12 (both etiology unknown), and in esophageal
355 adenocarcinomas, we see an increase in SBS3 (double-strand break-repair) and a decrease

356 in SBS17 (etiology unknown).

357 The average signature activity change across cancers of the same type is most often
358 monotonic as a function of CCF. In other words, the activities of mutation processes
359 consistently either decrease or increase (**Figures 5B and S4**). CLLs and lung
360 adenocarcinomas initially exhibit a sharp change in signature activity when transitioning
361 from clonal to subclonal mutations, but activity of the signatures appears to remain stable
362 across multiple subclonal expansions (**Figure 5B**). In contrast, esophageal
363 adenocarcinomas show a steady decrease in SBS17 activity, while thyroid
364 adenocarcinomas often display a continuing increase in SBS2 and SBS13 (APOBEC)
365 activity. These patterns observed across samples are also consistent at the single-sample
366 level, for example in individual CLL samples (**Figure 5C**).

367 Interestingly, the SBS9 activity changes in CLL and B-cell non-Hodgkin lymphoma reflect
368 the anatomical journey B cells have undergone in their evolution to cancers. Tumors
369 showing SBS9 (pol η associated with AID activity) activity originate from post-germinal
370 center B cells (Seifert et al., 2012). In these cases, SBS9 contributes to clonal but not
371 subclonal mutations, because only the tumor-founding cell was exposed to somatic
372 hypermutation in the germinal center. Later cells in this lineage have left the germinal
373 center and are no longer exposed to AID. Similarly, the strong decrease of SBS7 (UV light)
374 activity in cutaneous melanoma cases suggests these tumors have progressed to invade
375 inner layers of the skin (Breslow, 1970), out of reach of damaging UVB exposure (Dupont
376 et al., 2013). Finally, the co-occurring decrease of SBS4 (smoking) and increase of
377 SBS2/13 (APOBEC) activity suggests that in lung cancers, cell-intrinsic mutation
378 processes take over after early tumor evolution is fueled by external mutagens (Jamal-
379 Hanjani et al., 2017).

380

381 **Mutation signature activity changes mark subclonal boundaries**

382 We next compared the mutation signature change points (shifts in activity) with the CCF
383 of detected subclones, reasoning that these would correspond well if the emergence of
384 subclones is associated with changes in mutation process activity. In such a scenario, we

385 expect that the signature change points coincide with the CCF boundaries between
386 subclones, assuming that clustering partitioned the SNVs accurately. In accordance with
387 previous studies that highlight changes in signature activity between clonal and subclonal
388 mutations (Jamal-Hanjani et al., 2017; McGranahan et al., 2015), we find that 34.5-54.7%
389 of clone–subclone boundaries and 34.5%-57.3% of subclone-subclone boundaries coincide
390 with a signature change point (**Figure 5D, STAR Methods**). This not only validates our
391 clustering approach, but also demonstrates that subclonal expansions are often associated
392 with changes in signature activity. It further suggests that increased ITH would correspond
393 to greater activity change. Indeed, the samples with the largest changes in activity tend to
394 be the most heterogeneous (**Figure 5E**). Conversely, an average of 0.49 changes per sample
395 are not within a window of subclonal boundaries (**Figures 5F-G**), suggesting that some
396 detected CCF clusters represent multiple subclonal lineages (**STAR Methods**), consistent
397 with our mutation phasing results above.

398

399 **The landscape of subclonal driver mutations**

400 We leveraged the comprehensive whole-genome view of driver events across these cancer
401 genomes (Rheinbay et al., 2020) to gain insight into clonal *vs.* subclonal driver SNVs,
402 indels and SVs. Out of 5,414 high-confidence SNV and indel driver mutations in 389
403 genes, we found 385 (7.1%) subclonal driver mutations across 147 distinct genes (**Figure**
404 **6A**). In total, 86% of samples with at least one subclone (1,576/1,831) contain no identified
405 subclonal driver SNVs or indels, and only 11% of all detected subclones (280/2,542) were
406 associated with acquisition of a clear subclonal driver SNV or indel. In contrast, clonal
407 driver SNVs or indels were detected in 77% of samples (1,812/2,367).

408 As our whole-genome sequencing approach also allowed us to assess the clonality of SVs
409 (Cmero et al., 2020), we next sought to examine the clonality of SV drivers. We considered
410 an SV to be a driver if it was associated with a region of significantly recurrent breakpoints
411 (Rheinbay et al., 2020) at non-fragile sites. By this analysis, 56.9% of samples analyzed
412 (825/1,450) have a clonal SV driver, 14.7% (213/1,450) have at least one subclonal SV
413 driver (**Figure 6A**), and 6.1% (89/1,450) have exclusively subclonal SV drivers. Pilocytic

414 astrocytomas, non-Hodgkin's lymphomas, biliary adenocarcinomas, and thyroid
415 adenocarcinomas showed no evidence of subclonal SV drivers, while the remaining 26 of
416 30 cancer types analyzed all contained at least one subclonal SV driver in this cohort.

417 One explanation for the relative dearth of subclonal driver mutations is that subclonal
418 driver mutations have a lower population prevalence than clonal ones. Specifically, driver
419 identification depends on prevalence of the mutation within the cancer cohort. Our previous
420 analysis demonstrated that the most prevalent drivers are also those that occur earliest in
421 tumor development (Gerstung et al., 2020). This suggests that methods to annotate
422 mutations (or genes) as drivers would be particularly prone to missing subclonal driver
423 mutations. As such, we adapted a strategy from population genetics, to assess whether there
424 was subclonal selection, even in the absence of discernible subclonal drivers. Selective
425 pressures acting on the coding regions of cancer genomes can be quantified using the dN/dS
426 ratio, which compares the rates of non-synonymous and synonymous mutations
427 (Martincorena et al., 2017). A dN/dS ratio larger than 1 indicates positive selection, while
428 smaller ratios characterize negative selection, and dN/dS ≈ 1 points towards neutral
429 evolutionary dynamics. Previously, dN/dS > 1, evidence of positive selection, has been
430 shown for cancer driver genes in all somatic mutations (Martincorena et al., 2017). When
431 analyzing clonal mutations separately in our dataset, we confirm this signature of selection
432 within a set of 566 well-established driver genes (**STAR Methods**). When specifically
433 assaying our consensus subclonal mutations for the same set of drivers, we observe
434 dN/dS > 1 for nonsense, missense and splice-site SNVs (**Figure 6B**). This indicates that
435 selection for driver mutations, rather than neutral evolutionary dynamics (Williams et al.,
436 2016), frequently shapes subclonal expansions, in agreement with our earlier study
437 (Tarabichi et al., 2018). However, when considering dN/dS ratios for individual cancer
438 types, we observe that in only a subset, the 95% confidence intervals exceed the threshold
439 of positive selection (**Figure 6C**). The cancer types with evidence for selection had a
440 significantly higher number of tumors sequenced ($P = 1.6\times10^{-3}$, Mann-Whitney U test),
441 suggesting that the absence of conclusive signal in the remaining cancer types may be due
442 to statistical power limitations.

443 The driver SNV and indel landscape indicates that specific genes recurrently harbor

444 subclonal driver mutations across cancer types (**Figure 6A**). For example, the *SETD2*
445 tumor suppressor is frequently subclonally mutated in clear cell renal cell carcinomas, as
446 previously observed in multi-region sequencing experiments (Gerlinger et al., 2012), and
447 in pancreatic neuroendocrine cancers. Interestingly, mutations in some driver genes that
448 are exclusively clonal in most cancer types, are observed subclonally in others. For
449 example, we find subclonal driver mutations in *MEN1* in pancreatic neuroendocrine tumors
450 (6/30); *TP53* in prostate and breast cancers (4/12 and 5/59 respectively); and *CDKN2A* in
451 pancreatic adenocarcinomas (5/42). Gene set analysis (**STAR Methods**) revealed an
452 enrichment of subclonal mutations in genes responsible for chromatin remodeling,
453 suggesting an important role of these processes in subclonal variegation. Indeed, we find
454 that e.g. *ARID1A*, *PBRM1*, *KMT2C/D* and *SETD2* are enriched for subclonal driver
455 mutations. Other genes often mutated in subclones are splicing factor *SF3B1* and, in breast
456 and pancreatic adenocarcinomas, tumor suppressor *SMAD4*.

457 We similarly observed substantial variation in SV driver clonality across cancer types,
458 implying cancer type-specific roles for SVs during tumor evolution (**Figure 6A**). Ten
459 cancer types have a significant clonal bias for SV drivers (**Figure 6A**), when matched for
460 power, suggesting that these cancers are driven by early SV events. These include SVs in
461 the genomic region around *KIAA1549* in pilocytic astrocytomas, which likely result in the
462 *BRAF-KIAA1549* fusion gene (Faulkner et al., 2015). Ovarian adenocarcinoma and soft-
463 tissue leiomyosarcoma show the highest rates of SV driver subclonality (33.7% and 40.0%
464 respectively).

465 No significant subclonal enrichment was observed for SV drivers within a tumor type.
466 However, enrichment was observed for specific SV drivers across cancer types (**Figures**
467 **6A and S5**). Clonally enriched SV drivers (**Figure 6A**, q-value < 0.05, rank-based
468 permutation test) include those involving the *IGH* locus (97% of which occurred in
469 lymphomas), or targeting *CDK12*, *TERT*, *MDM2*, *CDKN2A, LRP5/PPP6R3*, *MYC, EGFR*
470 and gene poor region 8p11.21. In contrast, subclonally enriched SV drivers include those
471 targeting *RB1*, *AKR1C1/2/3*, *KLF5*, *PTEN* and the gene poor 5p12 region. Interestingly,
472 previous studies have linked *RB1* loss to tumor progression in liver (Bollard et al., 2017),
473 liposarcoma (Schneider-Stock et al., 2002; Takahira et al., 2005), and breast cancer

474 (Condorelli et al., 2017).

475 To further understand the clonality of gain-of-function driver SVs across cancer types, we
476 specifically focused on previously known and curated oncogenic driver fusion SVs (**STAR**
477 **Methods**). We found that known driver fusions are more likely to be clonal compared to
478 other SVs ($p = 0.0284$, Fisher's exact test, **Figure 6D**), with some recurrent fusions
479 appearing exclusively clonal or highly enriched for clonal events (*CCDC6-RET*, *BRAF-*
480 *KIAA1549*, *TMPRSS2-ERG*), pointing to a model where gain-of-function SVs tend to
481 appear early rather than late during tumor development.

482 Finally, to assess the potential impact of ITH on clinical decisions, we evaluated the
483 clonality of actionable subclonal driver mutations, reasoning that targeting mutations that
484 are not present in all tumor cells will likely result in ineffective treatment (Schmitt et al.,
485 2016). Restricting our analysis to genes and mutations for which inhibitors are available,
486 we find that 60.1% of tumors have at least one clinically actionable event (**Figure 6E**). Of
487 these, 9.7% contain at least one subclonal actionable driver, and 4.7% show only subclonal
488 actionable events. As our results represent conservative lower bound estimates of the
489 subclonality at the level of the whole tumor, these results reinforce the importance of
490 assessing the clonality of actionable mutations.

491 **DISCUSSION**

492 We have developed consensus approaches to characterize genome-wide ITH for 38 cancer
493 types, building on high quality SNVs, indels, SVs, CNAs, and curated driver mutations and
494 mutation signatures, leveraging the largest set of whole-genome sequenced tumor samples
495 compiled and analyzed to date. Remarkably, although these single region-based results are
496 conservative and place a lower bound estimate on ITH, we detect subclonal tumor cell
497 populations in 95.1% of 1,705 tumors. Individual subclones in the same tumor frequently
498 exhibit differential activity of mutation signatures, implying that subclonal expansions can
499 act as witnesses of temporally and spatially changing mutation processes. We extensively
500 characterized the clonality of SNVs, indels, SVs, and CNAs. For SNVs and indels, we
501 identified patterns of subclonal driver mutations in known cancer genes and average rates
502 of subclonal driver events per tumor (Jamal-Hanjani et al., 2017; Landau et al., 2013;
503 McGranahan et al., 2015; Yates et al., 2015). For SVs, we analyzed both candidate driver
504 and passenger events, revealing how SVs influence tumor initiation and progression.
505 Clonality estimates from CNAs suggest a complementary role of chromosomal instability
506 and mutagenic processes in driving subclonal expansions. Finally, our results show rich
507 subclonal architectures, with both linear and branching evolution in many cancers.

508 Analysis of dN/dS ratios in subclonal SNVs falling in exons of known cancer genes
509 revealed clear signs of positive selection across the detected subclones and across cancer
510 types. Although our analyses do not exclude the possibility that a small fraction of tumors
511 evolve under weak or no selection, they show that selection is widespread across cancer
512 types. Recent methodological advances to quantify selection in individual tumors from
513 explicit tumor growth models have emerged and could shed further light on the
514 evolutionary dynamics of individual tumors through single (Williams et al., 2018) and
515 multiple (Sun et al., 2017) tumor biopsies. Our findings extend Peter Nowell's model of
516 clonal evolution (Nowell, 1976): as neoplastic cells proliferate under chromosomal and
517 genetic instability, some of their daughter cells acquire mutations that convey further
518 selective advantages, allowing them to become precursors for new subclonal lineages.
519 Here, we have demonstrated that selection is ongoing up to and beyond diagnosis, in
520 virtually all tumors and cancer types. The ubiquiotous presence of subclones provides

521 evidence for ongoing selective sweeps, and akin to results of multi-region-based studies,
522 we also detect widespread branching evolution, implying co-existence and competition of
523 subclones.

524 Our observations highlight a considerable gap in knowledge about the drivers of subclonal
525 expansions. Specifically, only 11% of the 2,542 detected subclones have a currently known
526 SNV or indel driver mutation. Thus, late tumor development is either driven largely by
527 different mechanisms (copy number alterations, genomic rearrangements (Jamal-Hanjani
528 et al., 2017; Mamlouk et al., 2017), or epigenetic alterations), or most late driver mutations
529 remain to be discovered. In support of the latter, our recent study (Gerstung et al., 2020)
530 finds that late driver mutations occur in a more diverse set of genes than early drivers. For
531 now, the landscape of subclonal driver mutations in localized cancer remains largely
532 unexplored, in part due to limited resolution and statistical power to detect recurrence of
533 subclonal drivers. Nonetheless, each tumor type has its own characteristic patterns of
534 subclonal SNVs, indels, SVs and CNAs, revealing distinct evolutionary narratives. Tumor
535 evolution does not end with the last complete clonal expansion, and it is therefore important
536 to account for ITH and its drivers in clinical studies.

537 We show that regions of recurrent genomic rearrangements, harboring likely driver SVs,
538 also exhibit subclonal rearrangements. This suggests that improved annotations must be
539 sought for both SVs and SNVs, in order to comprehensively catalogue the drivers of
540 subclonal expansion. By combining analysis of SV clonality with improved annotations of
541 candidate SV drivers (Rheinbay et al., 2020), we highlight tumor types that would benefit
542 from further characterization of subclonal SV drivers, such as pancreatic neuroendocrine
543 cancers and leiomyosarcomas.

544 These observations have a number of promising clinical implications. For example, there
545 is subclonal enrichment for SVs causing *RB1* loss across multiple cancer types, expanding
546 on the known behavior of *RB1* mutations in breast cancer (Condorelli et al., 2017). These
547 SVs may be linked to known resistance mechanisms to emerging treatments (*e.g.* CDK4/6
548 inhibitors in breast (Condorelli et al., 2017) and bladder (Pan et al., 2017) cancer). If
549 profiled in a resistance setting, they may provide a pathway to second-line administration
550 of cytotoxic therapies such as cisplatin or ionizing radiation, which show improved efficacy

551 in tumors harboring *RB1* loss (Knudsen and Knudsen, 2008).

552 Our study builds upon a wealth of data of cancer whole-genome sequences generated under
553 the auspices of the International Cancer Genome Consortium and The Cancer Genome
554 Atlas, allowing detailed characterization of ITH from single tumor samples across 38
555 cancer types. It builds a consensus reconstruction of CNAs from 6 methods and consensus
556 subclonal reconstruction from 11 methods. In establishing this reconstruction, we found
557 that each individual method makes errors that are corrected by the consensus. Our
558 consensus-building tools and techniques thus provide a set of best practices for future
559 analyses of tumor whole-genome sequencing data. In addition, our high-quality curated
560 consensus subclonal reconstructions on 2,658 tumor whole genomes spanning 38 cancer
561 types constitute a rich resource for future studies.

562 # STAR METHODS SUMMARY

563 **Consensus copy number analysis**

564 As the basis for our subclonal architecture reconstruction, we needed a confident copy
565 number profile for each sample. To this end, we applied six copy number analysis methods
566 (ABSOLUTE, ACEseq, Battenberg, cloneHD, JaBbA and Sclust) and combined their
567 results into a robust consensus (see **STAR Methods** for details). In brief, each individual
568 method segments the genome into regions with constant copy number, then calculates the
569 copy number of both alleles for the genomic location. Some of the methods further
570 distinguish between clonal and subclonal copy number states, *i.e.* a mixture of two or more
571 copy number states within a genomic region. Disagreement between methods mostly stems
572 from either difference in the segmentation step, or uncertainty on whole genome
573 duplication (WGD) status. Both issues were resolved using our consensus strategy.

574 To identify a set of consensus breakpoints, we combined the breakpoints reported by the
575 CNA methods with the consensus structural variants (SVs). If a hotspot of copy number
576 breakpoints could be explained by an SV, we removed the copy number breakpoints in
577 favor of the base-pair resolution SV. The remaining hotspots were merged into consensus
578 calls to complement the SV-based breakpoints. This combined breakpoint set was then
579 used as input to all methods in a second pass, where methods were required to strictly
580 adhere to the provided breakpoints.

581 Allele-specific copy number states were resolved by assessing agreement between outputs
582 of the individual callers. A consensus purity for each sample was obtained by combining
583 the estimates of the copy number methods with the results of the subclonal architecture
584 reconstruction methods that infer purity using only SNVs.

585 Each copy number segment of the consensus output was rated with a star-ranking
586 representing confidence.

587 To create a subclonal copy number consensus, we used three of the copy number methods
588 that predicted subclonal states for segments and flagged the segment as subclonal when at
589 least two methods agreed the segment represented subclonal copy number.

590 **Consensus subclonal architecture clustering**

591 We applied 11 subclonal reconstruction methods (BayClone-C, Ccube, CliP, cloneHD,
592 CTPsingle, DPClust, PhylogicNDT, PhyloWGS, PyClone, Sclust, SVclone). Most were
593 developed or further optimized during this study. Their outputs were combined into a
594 robust consensus subclonal architecture (see **STAR Methods** for details). During this
595 procedure, we used the PCAWG consensus SNVs and indels [Synapse ID syn7118450]
596 and SVs [syn7596712].

597 The procedure to create consensus architectures consisted of three phases: a run of the 11
598 callers on a subset of SNVs that reside on copy number calls of high-confidence, merging
599 of the output of the callers into a consensus and finally assignment of all SNVs, indels and
600 SVs.

601 Each of the 11 subclonal reconstruction callers outputs the number of mutation clusters per
602 tumor, the number of mutations in each cluster, and the clusters' proportion of (tumor) cells
603 (cancer cell fraction, CCF). These data were used as input to three orthogonal approaches
604 to create a consensus: WeMe, CSR and CICC. The results reported in this paper are from
605 the WeMe consensus method, but all three developed methods lead to similar results, and
606 were used to validate each other (**STAR Methods**).

607 The consensus subclonal architecture was compared to the individual methods on two
608 independent simulation sets, one 500-sample for training and one 965-sample for
609 validation, and on the real PCAWG samples to evaluate robustness. The metrics by which
610 methods were scored account for the fraction of clonal mutations, number of mutation
611 clusters and the root mean square error (RMSE) of mutation assignments. To calculate the
612 overall performance of a method, ranks of the three metrics were averaged per sample.

613 Across the two simulated datasets, the scores of the individual methods were variable,
614 whereas the consensus methods were consistently among the best across the range of
615 simulated number of subclones, tumor purity, tumor ploidy and sequencing depth. The
616 highest similarities were observed among the consensus and the best individual methods in
617 the simulation sets, and among the consensus methods in real data, suggesting stability of
618 the consensus in the real set. Increasing the number of individual methods input to the

619 consensus consistently improved performance and the highest performance was obtained
620 for the consensus run on the full 11 individual methods, suggesting that each individual
621 method has its own strengths that are successfully integrated by the consensus approaches
622 (**STAR Methods**).

623 All SNVs, indels and SVs were assigned to the clusters that were determined by the
624 consensus subclonal architecture using MutationTimer (Gerstung et al., 2020). Each
625 mutation cluster is modelled by a beta-binomial distribution and probabilities for each
626 mutation belonging to each cluster are calculated. This results in the final consensus
627 subclonal architecture, and in addition, it also timed mutations relative to copy number
628 gains (**STAR Methods**).

629

630 **SV clonality analysis**

631 Due to the difficulty in determining SV VAFs from short-read sequence data, and
632 subsequent CCF point estimation (Cmero et al., 2020), we elected to explore patterns of
633 putative driver SV clonality using subclonal *probabilities*, allowing us to account for
634 uncertainty in our observations of SV clonality (**STAR Methods**). After excluding
635 unpowered samples, highly mutated samples, and cancer types with less than ten powered
636 samples (**STAR Methods**), we analyzed 125,920 consensus SVs from 1,517 samples,
637 across 28 cancer types. SVs were divided into candidate driver SVs and candidate
638 passenger SVs using annotations from a companion paper (Rheinbay et al., 2020). SVs
639 were considered candidate drivers if they were annotated as having significantly recurrent
640 breakpoints (SRBs) at non-fragile sites, and candidate passenger SVs otherwise (**STAR**
641 **Methods**).

642 Subclonal probabilities of driver and passenger SVs across tumor types were observed
643 using weighted median and interquartile ranges (**STAR Methods**). Any tumor types with
644 interquartile ranges exceeding subclonal probabilities of 0.5 were considered as having
645 evidence of subclonal SVs. Permutation testing was used to determine significant
646 differences in the weighted medians between driver and passenger SVs (**STAR Methods**).
647 To test if any genomic loci were enriched for clonal or subclonal SVs across cancer types,

648 we employed a GSEA-like (Subramanian et al., 2005) rank-based permutation test (**STAR**
649 **Methods**).

650

651 **"Winner's curse" correction**

652 Because somatic mutation callers require a minimum coverage of supporting reads, in
653 samples with low purity and/or small subclones, the reported CCF values and cluster sizes
654 will be biased. As variants observed in a lower number of reads have a higher probability
655 to be missed by somatic mutation callers, rare subclones will show lower apparent mutation
656 numbers and higher apparent CCF values. We refer to this effect as the "Winner's curse".
657 To adjust mutation clusters both in size and in CCF, we developed two methods,
658 PhylogicCorrectBias and SpoilSport. Results from both methods were integrated to
659 produce a consensus correction, and our correction approach was validated on simulated
660 data (**STAR Methods**).

661

662 **Mutation signatures trajectory analysis**

663 Given the mutation signatures obtained from PCAWG [syn8366024], we used TrackSig
664 (Rubanova et al., 2020) to fit the evolutionary trajectories of signature activities. Mutations
665 were ordered by their approximate relative temporal order in the tumor, by calculating a
666 pseudo-time ordering using CCF and copy number. Time-ordered mutations were
667 subsequently binned to create time points on a pseudo-timeline to which signature
668 trajectories can be mapped.

669 At each time point, mutations were classified into 96 classes based on their trinucleotide
670 context and a mixture of multinomial distributions was fitted, each component describing
671 the distribution of one active signature. Derived mixture component coefficients
672 correspond to mutation signature activity values, reflecting the proportion of mutations in
673 a sample that were generated by a mutation process. By applying this approach to every
674 time point along the evolutionary timeline of a sample, a trajectory of the activity of
675 signatures over time was obtained.

676 We applied likelihood maximization and the Bayesian Information Criterion to simulations
677 to establish the optimal threshold at which signature activity changes can be detected. This
678 threshold was determined to be 6%. Subsequently, a pair of adjacent mutation bins was
679 marked as constituting a change in activity if the absolute difference in activity between
680 the bins of a at least one signature was greater than the threshold.

681 Signature trajectories were mapped to our subclonal reconstruction architectures by
682 dividing the CCF space according to the proportion of mutations per time point belonging
683 to a mutation cluster determined by the consensus reconstruction. By comparing distances
684 in pseudo-time between trajectory change points and cluster boundaries, change points
685 were classified as "supporting" a boundary if they are no more than three bins apart.

686 **REFERENCES**

687 Alexandrov, L.B., Kim, J., Haradhvala, N.J., Huang, M.N., Tian Ng, A.W., Wu, Y., Boot,
688 A., Covington, K.R., Gordenin, D.A., Bergstrom, E.N.*, et al.* (2020). The repertoire of
689 mutational signatures in human cancer. Nature *578*, 94-101.

690 Andor, N., Graham, T.A., Jansen, M., Xia, L.C., Aktipis, C.A., Petritsch, C., Ji, H.P., and
691 Maley, C.C. (2016). Pan-cancer analysis of the extent and consequences of intratumor
692 heterogeneity. Nat Med *22*, 105-113.

693 Aran, D., Sirota, M., and Butte, A.J. (2015). Systematic pan-cancer analysis of tumour
694 purity. Nat Commun *6*, 8971.

695 Bollard, J., Miguela, V., Ruiz de Galarreta, M., Venkatesh, A., Bian, C.B., Roberto, M.P.,
696 Tovar, V., Sia, D., Molina-Sanchez, P., Nguyen, C.B.*, et al.* (2017). Palbociclib (PD-
697 0332991), a selective CDK4/6 inhibitor, restricts tumour growth in preclinical models of
698 hepatocellular carcinoma. Gut *66*, 1286-1296.

699 Brastianos, P.K., Nayyar, N., Rosebrock, D., Leshchiner, I., Gill, C.M., Livitz, D.,
700 Bertalan, M.S., D'Andrea, M., Hoang, K., Aquilanti, E.*, et al.* (2017). Resolving the
701 phylogenetic origin of glioblastoma via multifocal genomic analysis of pre-treatment and
702 treatment-resistant autopsy specimens. npj Precision Oncology *1*, 33.

703 Breslow, A. (1970). Thickness, cross-sectional areas and depth of invasion in the prognosis
704 of cutaneous melanoma. Ann Surg *172*, 902-908.

705 Campbell, P.J., Pleasance, E.D., Stephens, P.J., Dicks, E., Rance, R., Goodhead, I.,
706 Follows, G.A., Green, A.R., Futreal, P.A., and Stratton, M.R. (2008). Subclonal
707 phylogenetic structures in cancer revealed by ultra-deep sequencing. Proc Natl Acad Sci U
708 S A *105*, 13081-13086.

709 Carter, S.L., Cibulskis, K., Helman, E., McKenna, A., Shen, H., Zack, T., Laird, P.W.,
710 Onofrio, R.C., Winckler, W., Weir, B.A.*, et al.* (2012). Absolute quantification of somatic
711 DNA alterations in human cancer. Nat Biotechnol *30*, 413-421.

712 Cmero, M., Yuan, K., Ong, C.S., Schroder, J., Corcoran, N.M., Papenfuss, T., Hovens,
713 C.M., Markowetz, F., and Macintyre, G. (2020). Inferring structural variant cancer cell
714 fraction. Nat Commun *11*, 730.

715 Condorelli, R., Spring, L., O'Shaughnessy, J., Lacroix, L., Bailleux, C., Scott, V., Dubois,
716 J., Nagy, R.J., Lanman, R.B., Iafrate, A.J.*, et al.* (2017). Polyclonal RB1 mutations and
717 acquired resistance to CDK 4/6 inhibitors in patients with metastatic breast cancer. Ann
718 Oncol.

719 de Bruin, E.C., McGranahan, N., Mitter, R., Salm, M., Wedge, D.C., Yates, L., Jamal-
720 Hanjani, M., Shafi, S., Murugaesu, N., Rowan, A.J.*, et al.* (2014). Spatial and temporal
721 diversity in genomic instability processes defines lung cancer evolution. Science *346*, 251-
722 256.

723 Dentro, S.C., Wedge, D.C., and Van Loo, P. (2017). Principles of Reconstructing the
724 Subclonal Architecture of Cancers. Cold Spring Harb Perspect Med *7*.

725 Dupont, E., Gomez, J., and Bilodeau, D. (2013). Beyond UV radiation: a skin under
726 challenge. Int J Cosmet Sci *35*, 224-232.

727 Espiritu, S.M.G., Liu, L.Y., Rubanova, Y., Bhandari, V., Holgersen, E.M., Szyca, L.M.,
728 Fox, N.S., Chua, M.L.K., Yamaguchi, T.N., Heisler, L.E.*, et al.* (2018). The Evolutionary
729 Landscape of Localized Prostate Cancers Drives Clinical Aggression. Cell *173*, 1003-1013
730 e1015.

731 Faulkner, C., Ellis, H.P., Shaw, A., Penman, C., Palmer, A., Wragg, C., Greenslade, M.,
732 Haynes, H.R., Williams, H., Lowis, S.*, et al.* (2015). BRAF Fusion Analysis in Pilocytic
733 Astrocytomas: KIAA1549-BRAF 15-9 Fusions Are More Frequent in the Midline Than
734 Within the Cerebellum. J Neuropathol Exp Neurol *74*, 867-872.

735 Garraway, L.A., and Lander, E.S. (2013). Lessons from the cancer genome. Cell *153*, 17-
736 37.

737 Gerlinger, M., Rowan, A.J., Horswell, S., Math, M., Larkin, J., Endesfelder, D., Gronroos,
738 E., Martinez, P., Matthews, N., Stewart, A.*, et al.* (2012). Intratumor heterogeneity and
739 branched evolution revealed by multiregion sequencing. N Engl J Med *366*, 883-892.

740 Gerstung, M., Jolly, C., Leshchiner, I., Dentro, S.C., Gonzalez, S., Rosebrock, D., Mitchell,
741 T.J., Rubanova, Y., Anur, P., Yu, K., *et al.* (2020). The evolutionary history of 2,658
742 cancers. Nature *578*, 122-128.

743 Greaves, M., and Maley, C.C. (2012). Clonal evolution in cancer. Nature *481*, 306-313.

744 Gundem, G., Van Loo, P., Kremeyer, B., Alexandrov, L.B., Tubio, J.M.C., Papaemmanuil,
745 E., Brewer, D.S., Kallio, H.M.L., Hognas, G., Annala, M., *et al.* (2015). The evolutionary
746 history of lethal metastatic prostate cancer. Nature *520*, 353-357.

747 Hiley, C., de Bruin, E.C., McGranahan, N., and Swanton, C. (2014). Deciphering
748 intratumor heterogeneity and temporal acquisition of driver events to refine precision
749 medicine. Genome Biol *15*, 453.

750 Jamal-Hanjani, M., Wilson, G.A., McGranahan, N., Birkbak, N.J., Watkins, T.B.K.,
751 Veeriah, S., Shafi, S., Johnson, D.H., Mitter, R., Rosenthal, R., *et al.* (2017). Tracking the
752 Evolution of Non-Small-Cell Lung Cancer. N Engl J Med *376*, 2109-2121.

753 Kim, J., Mouw, K.W., Polak, P., Braunstein, L.Z., Kamburov, A., Kwiatkowski, D.J.,
754 Rosenberg, J.E., Van Allen, E.M., D'Andrea, A., and Getz, G. (2016). Somatic ERCC2
755 mutations are associated with a distinct genomic signature in urothelial tumors. Nat Genet
756 *48*, 600-606.

757 Knudsen, E.S., and Knudsen, K.E. (2008). Tailoring to RB: tumour suppressor status and
758 therapeutic response. Nat Rev Cancer *8*, 714-724.

759 Landau, D.A., Carter, S.L., Stojanov, P., McKenna, A., Stevenson, K., Lawrence, M.S.,
760 Sougnez, C., Stewart, C., Sivachenko, A., Wang, L., *et al.* (2013). Evolution and impact of
761 subclonal mutations in chronic lymphocytic leukemia. Cell *152*, 714-726.

762 Maley, C.C., Galipeau, P.C., Finley, J.C., Wongsurawat, V.J., Li, X., Sanchez, C.A.,
763 Paulson, T.G., Blount, P.L., Risques, R.A., Rabinovitch, P.S., *et al.* (2006). Genetic clonal
764 diversity predicts progression to esophageal adenocarcinoma. Nat Genet *38*, 468-473.

765 Maley, C.C., Galipeau, P.C., Li, X., Sanchez, C.A., Paulson, T.G., Blount, P.L., and Reid,
766 B.J. (2004). The combination of genetic instability and clonal expansion predicts
767 progression to esophageal adenocarcinoma. Cancer Res *64*, 7629-7633.

768 Mamlouk, S., Childs, L.H., Aust, D., Heim, D., Melching, F., Oliveira, C., Wolf, T., Durek,
769 P., Schumacher, D., Blaker, H., *et al.* (2017). DNA copy number changes define spatial
770 patterns of heterogeneity in colorectal cancer. Nat Commun *8*, 14093.

771 Martincorena, I., Raine, K.M., Gerstung, M., Dawson, K.J., Haase, K., Van Loo, P.,
772 Davies, H., Stratton, M.R., and Campbell, P.J. (2017). Universal Patterns of Selection in
773 Cancer and Somatic Tissues. Cell *171*, 1029-1041 e1021.

774 McGranahan, N., Favero, F., de Bruin, E.C., Birkbak, N.J., Szallasi, Z., and Swanton, C.
775 (2015). Clonal status of actionable driver events and the timing of mutational processes in
776 cancer evolution. Sci Transl Med *7*, 283ra254.

777 McGranahan, N., and Swanton, C. (2017). Clonal Heterogeneity and Tumor Evolution:
778 Past, Present, and the Future. Cell *168*, 613-628.

779 McPherson, A., Roth, A., Laks, E., Masud, T., Bashashati, A., Zhang, A.W., Ha, G., Biele,
780 J., Yap, D., Wan, A., *et al.* (2016). Divergent modes of clonal spread and intraperitoneal
781 mixing in high-grade serous ovarian cancer. Nat Genet *48*, 758-767.

782 Mroz, E.A., and Rocco, J.W. (2013). MATH, a novel measure of intratumor genetic
783 heterogeneity, is high in poor-outcome classes of head and neck squamous cell carcinoma.
784 Oral Oncol *49*, 211-215.

785 Mroz, E.A., Tward, A.D., Pickering, C.R., Myers, J.N., Ferris, R.L., and Rocco, J.W.
786 (2013). High intratumor genetic heterogeneity is related to worse outcome in patients with
787 head and neck squamous cell carcinoma. Cancer *119*, 3034-3042.

788 Nik-Zainal, S., Van Loo, P., Wedge, D.C., Alexandrov, L.B., Greenman, C.D., Lau, K.W.,
789 Raine, K., Jones, D., Marshall, J., Ramakrishna, M., *et al.* (2012). The life history of 21
790 breast cancers. Cell *149*, 994-1007.

791 Nowell, P.C. (1976). The clonal evolution of tumor cell populations. Science *194*, 23-28.

792 Pan, Q., Sathe, A., Black, P.C., Goebell, P.J., Kamat, A.M., Schmitz-Draeger, B., and
793 Nawroth, R. (2017). CDK4/6 Inhibitors in Cancer Therapy: A Novel Treatement Strategy
794 for Bladder Cancer. Bladder Cancer *3*, 79-88.

795 Rheinbay, E., Nielsen, M.M., Abascal, F., Wala, J.A., Shapira, O., Tiao, G., Hornshoj, H.,
796 Hess, J.M., Juul, R.I., Lin, Z., *et al.* (2020). Analyses of non-coding somatic drivers in
797 2,658 cancer whole genomes. Nature *578*, 102-111.

798 Rocco, J.W. (2015). Mutant allele tumor heterogeneity (MATH) and head and neck
799 squamous cell carcinoma. Head Neck Pathol *9*, 1-5.

800 Rubanova, Y., Shi, R., Harrigan, C.F., Li, R., Wintersinger, J., Sahin, N., Deshwar, A., and
801 Morris, Q. (2020). Reconstructing evolutionary trajectories of mutation signature activities
802 in cancer using TrackSig. Nat Commun *11*, 731.

803 Salcedo, A., Tarabichi, M., Espiritu, S.M.G., Deshwar, A.G., David, M., Wilson, N.M.,
804 Dentro, S., Wintersinger, J.A., Liu, L.Y., Ko, M., *et al.* (2020). A community effort to
805 create standards for evaluating tumor subclonal reconstruction. Nat Biotechnol *38*, 97-107.

806 Schmitt, M.W., Loeb, L.A., and Salk, J.J. (2016). The influence of subclonal resistance
807 mutations on targeted cancer therapy. Nat Rev Clin Oncol *13*, 335-347.

808 Schneider-Stock, R., Boltze, C., Jaeger, V., Stumm, M., Seiler, C., Rys, J., Schütze, K.,
809 and Roessner, A. (2002). Significance of loss of heterozygosity of the RB1 gene during
810 tumour progression in well-differentiated liposarcomas. The Journal of Pathology *197*,
811 654-660.

812 Seifert, M., Sellmann, L., Bloehdorn, J., Wein, F., Stilgenbauer, S., Durig, J., and Kuppers,
813 R. (2012). Cellular origin and pathophysiology of chronic lymphocytic leukemia. J Exp
814 Med *209*, 2183-2198.

815 Shaw, A.T., Friboulet, L., Leshchiner, I., Gainor, J.F., Bergqvist, S., Brooun, A., Burke,
816 B.J., Deng, Y.L., Liu, W., Dardaei, L., *et al.* (2016). Resensitization to Crizotinib by the
817 Lorlatinib ALK Resistance Mutation L1198F. N Engl J Med *374*, 54-61.

818 Sottoriva, A., Spiteri, I., Piccirillo, S.G., Touloumis, A., Collins, V.P., Marioni, J.C.,
819 Curtis, C., Watts, C., and Tavare, S. (2013). Intratumor heterogeneity in human
820 glioblastoma reflects cancer evolutionary dynamics. Proc Natl Acad Sci U S A *110*, 4009-
821 4014.

822 Stratton, M.R., Campbell, P.J., and Futreal, P.A. (2009). The cancer genome. Nature *458*,
823 719-724.

824 Subramanian, A., Tamayo, P., Mootha, V.K., Mukherjee, S., Ebert, B.L., Gillette, M.A.,
825 Paulovich, A., Pomeroy, S.L., Golub, T.R., Lander, E.S.*, et al.* (2005). Gene set enrichment
826 analysis: A knowledge-based approach for interpreting genome-wide expression profiles.
827 Proceedings of the National Academy of Sciences *102*, 15545-15550.

828 Sun, R., Hu, Z., Sottoriva, A., Graham, T.A., Harpak, A., Ma, Z., Fischer, J.M., Shibata,
829 D., and Curtis, C. (2017). Between-region genetic divergence reflects the mode and tempo
830 of tumor evolution. Nat Genet *49*, 1015-1024.

831 Tabin, C.J., Bradley, S.M., Bargmann, C.I., Weinberg, R.A., Papageorge, A.G., Scolnick,
832 E.M., Dhar, R., Lowy, D.R., and Chang, E.H. (1982). Mechanism of activation of a human
833 oncogene. Nature *300*, 143-149.

834 Takahira, T., Oda, Y., Tamiya, S., Yamamoto, H., Kobayashi, C., Izumi, T., Ito, K.,
835 Iwamoto, Y., and Tsuneyoshi, M. (2005). Alterations of the RB1 gene in dedifferentiated
836 liposarcoma. Mod Pathol *18*, 1461-1470.

837 Tarabichi, M., Martincorena, I., Gerstung, M., Leroi, A.M., Markowetz, F., Spellman, P.T.,
838 Morris, Q.D., Lingjaerde, O.C., Wedge, D.C., and Van Loo, P. (2018). Neutral tumor
839 evolution? Nat Genet *50*, 1630-1633.

840 The ICGC/TCGA Pan-Cancer Analysis of Whole Genomes Consortium (2020). Pan-
841 cancer analysis of whole genomes. Nature *578*, 82-93.

842 Turajlic, S., Xu, H., Litchfield, K., Rowan, A., Chambers, T., Lopez, J.I., Nicol, D.,
843 O'Brien, T., Larkin, J., Horswell, S.*, et al.* (2018a). Tracking Cancer Evolution Reveals
844 Constrained Routes to Metastases: TRACERx Renal. Cell *173*, 581-594 e512.

845 Turajlic, S., Xu, H., Litchfield, K., Rowan, A., Horswell, S., Chambers, T., O'Brien, T.,
846 Lopez, J.I., Watkins, T.B.K., Nicol, D.*, et al.* (2018b). Deterministic Evolutionary
847 Trajectories Influence Primary Tumor Growth: TRACERx Renal. Cell *173*, 595-610 e511.

848 Van Loo, P., Nordgard, S.H., Lingjaerde, O.C., Russnes, H.G., Rye, I.H., Sun, W.,
849 Weigman, V.J., Marynen, P., Zetterberg, A., Naume, B., *et al.* (2010). Allele-specific copy
850 number analysis of tumors. Proc Natl Acad Sci U S A *107*, 16910-16915.

851 Vogelstein, B., Papadopoulos, N., Velculescu, V.E., Zhou, S., Diaz, L.A., Jr., and Kinzler,
852 K.W. (2013). Cancer genome landscapes. Science *339*, 1546-1558.

853 Williams, M.J., Werner, B., Barnes, C.P., Graham, T.A., and Sottoriva, A. (2016).
854 Identification of neutral tumor evolution across cancer types. Nat Genet *48*, 238-244.

855 Williams, M.J., Werner, B., Heide, T., Curtis, C., Barnes, C.P., Sottoriva, A., and Graham,
856 T.A. (2018). Quantification of subclonal selection in cancer from bulk sequencing data.
857 Nat Genet *50*, 895-903.

858 Yates, L.R., Gerstung, M., Knappskog, S., Desmedt, C., Gundem, G., Van Loo, P., Aas,
859 T., Alexandrov, L.B., Larsimont, D., Davies, H., *et al.* (2015). Subclonal diversification of
860 primary breast cancer revealed by multiregion sequencing. Nat Med *21*, 751-759.

861

862 # FIGURE LEGENDS

863 **Figure 1. Consensus-based characterization of intra-tumor heterogeneity.**

864 (A) Schematic representation of our consensus-based intra-tumor heterogeneity (ITH)
865 reconstruction from sequencing data. (B) Samples with and without whole-genome
866 duplications separate in two clusters according to their consensus ploidy and the fraction
867 of the genome showing loss of heterozygosity. (C) Agreement between the six copy
868 number callers using a multi-tier consensus copy number calling approach. The three lines
869 denote the fraction of the genome at which agreement is reached at different levels of
870 confidence: (near-)complete agreement on both alleles of clonal copy number, a strict
871 majority agreement on both alleles of clonal copy number and (near-)complete or strict
872 majority agreement on both alleles of rounded subclonal copy number (see **STAR**
873 **Methods**). At the third level, agreement is reached on an average 93% of the genome. (D)
874 Heatmap of the normalized average pairwise similarities of subclonal architectures
875 identified by 11 individual, 3 consensus, and 3 control reconstruction methods. Each
876 method is represented by one colored square on the diagonal. On rows and columns, each
877 method is compared to all other methods. The upper triangle shows the average pairwise
878 similarities on the 2,778 PCAWG samples, the lower triangle shows the same on a
879 validation set of 965 simulated samples. In the leftmost column similarities are computed
880 against the truth of the simulated set. Color intensities scale with the similarities and were
881 normalized separately for PCAWG, simulations and truth.

882

883 **Figure 2. Winner's curse correction.**

884 (A) Validation of our approach to adjust for the "winner's curse-like effect, and (B-C) the
885 estimated cluster-CCF and mutation adjustment in all mutation clusters identified in the
886 study. Subclonal clusters show a shift to larger CCF values after correction (B) and the
887 majority of clusters are estimated to contain additional missed SNVs (C).

888

889

890 **Figure 3. Overview and characterization of ITH across cancer types.**

891 Evidence of ITH is shown for 1,705 samples with sufficient power to detect subclones at
892 CCF > 30% (see **STAR Methods**). Samples have been limited to those with less than 2%
893 tumor contamination in the matched normal sample and no activity of any of the identified
894 artefact signatures (Alexandrov et al., 2020). Only representative samples (The
895 ICGC/TCGA Pan-Cancer Analysis of Whole Genomes Consortium, 2020) from multi-
896 sample cases are shown. (A) Bar plot showing the fraction of samples with given number
897 of subclones; (B-E) Scatter plots showing the fractions of subclonal SNVs, indels, SVs and
898 subclonal arm-level CNAs (the latter two mutation types are only plotted for samples that
899 have at least 5 events, sample order is determined by increasing fraction of subclonal SNVs
900 and conserved in the other three panels); Violin plots showing the total mutation burden
901 (F) and overall fraction of the genome that does not have a copy number state of 1+1, or
902 2+2 in WGD samples (G); Heatmaps showing the fraction of tumor samples with whole
903 genome duplications (H) and the mean power to identify subclones per cancer types
904 (number of reads per clonal copy – nrpcc, see **STAR Methods)** (I)**.**

905

906 **Figure 4. Further characterization of ITH using mutation phasing.**

907 (A-B) Proportion of powered tumors with evidence of linear and branching phylogenies,
908 through analysis of phased reads of variants in-*cis* (A) or in-*trans* (B) among tumors with
909 at least one phaseable pair in the appropriate context. (C) Fraction of powered samples,
910 stratified by number of consensus subclones, with at least one linear or branching pair (χ^2-
911 test for independence). (D) Number of samples with linear or branching pairs when sets
912 are filtered to be comparable. Error bars indicate the 95% bootstrap interval. Samples are
913 colored by tumor type and boxed (orange) when they present with pairs of both types. (E)
914 Probabilities of observing a linear *vs.* branching relationship when picking two random
915 subclones from TRACERx 100 trees (Jamal-Hanjani et al., 2017). Error bars indicate the
916 95% bootstrap interval.

917

918 **Figure 5. Subclonal boundaries are associated with changes in mutation signature**
919 **activity.**

920 (A) Mutation signature changes across cancer types. Bar graphs show the proportion of
921 tumors in which signature (pairs) change and radial plots provide a view per cancer type.
922 Each radial plot contains the signatures that are active in at least 5 tumors and change (≥
923 6%) in at least 3 tumors. The left and right side of the radial plot represent signatures that
924 become less and more active, respectively. The height of a wedge represents the average
925 activity change (log scale), the color denotes the signature and the transparency shows the
926 fraction of tumors in which the signature changes (as a proportion of the tumors in which
927 the signature is active). Signatures are sorted around the radial plot (top-to-bottom) by
928 maximum average activity change. (B) Average signature trajectories for selected cancer
929 types. Each line is colored by signature and corresponds to the average activity across
930 tumors of this cancer type in which the signature is active. The width of the line represents
931 the number of tumors that are represented. Mutations are split into clonal and subclonal,
932 visually divided by a red vertical line. (C) Signature trajectories for selected individual
933 CLL tumors. Each line corresponds to an activity trajectory derived from a bootstrap
934 sample of SNVs. The grey vertical grid represents the mutation bins. These are colored
935 grey when a significant change in signature activity is detected. Red vertical lines represent
936 consensus subclonal mutation clusters. (D) The fraction of signature change points that
937 coincide with boundaries between mutation clusters, as compared to what is expected when
938 randomly placing change points. (E) The number of subclones detected in tumors grouped
939 by the maximum detected signature activity change. (F) An overview of coinciding SNV
940 cluster boundaries and signature activity change points. (G) The average number of
941 additional signature change points detected per tumor.

942

943 **Figure 6. Driver mutations and subclonal selection.**

944 (A) Heatmap of the fraction of samples of the different cancer types with clonal (orange)
945 and subclonal (blue) driver substitutions and indels (left panel) and structural variants (right
946 panel). Marginal bar plots represent the fraction of clonal and subclonal driver mutations

947 in each cancer type (side) and each driver gene or candidate region (top). Only genes with
948 at least 4 subclonal driver mutations are shown. For SNVs and indel drivers (top left panel),
949 gene set and pathway annotations highlight an enrichment of subclonally mutated drivers
950 in chromatin remodeling. (B) dN/dS values for clonal and subclonal SNVs in 566
951 established cancer genes across all primary tumors. Values for missense, nonsense, splice
952 site, and all mutations are shown, along with the 95% confidence intervals. (C) Cancer and
953 mutation types for which dN/dS is significantly greater than 1 (95% confidence
954 intervals>1) for clonal and subclonal mutations. Cancer types are ordered by the total
955 number of samples. (D) Proportions of (sub)clonal driver gene fusions versus non-driver
956 fusions. (E) Survey of targetable driver mutations across cancer types, stratified by clonal
957 status.

958 ## Supplementary Figure Legends

959 **Figure S1. Validation of consensus purity values.**

960 The lower triangle shows pairwise scatterplots of the purities obtained through expression
961 profiles of a panel of immune and stromal genes (ESTIMATE), somatic copy number data
962 (ABSOLUTE), leukocyte unmethylation (LUMP), image analysis by hematoxylin and
963 eosin staining (H&E staining), and consensus purity as derived by Aran *et al*. (Aran et al.,
964 2015) (CPE). The top triangle shows the respective Pearson correlation coefficients and
965 the number of samples that have both purity estimates available.

966

967 **Figure S2. Power analysis of the consensus subclonal architecture approach.**

968 (A) Our ability to detect subclones depends, not on the number of detected SNVs, but on
969 the number of reads per clonal copy (nrpcc) available. This metric takes tumor purity,
970 ploidy and sequencing coverage into account (see **STAR Methods**). We control for this
971 effect by including only tumors with nrpcc ≥ 10. In these tumors, we should be sufficiently
972 powered to detect a subclone at a CCF as low as 30% (see **STAR Methods**). This becomes
973 clear from (B) which shows the minimum CCF of the detected clusters in each tumor
974 against the number of reads per chromosome copy.

975

976 **Figure S3. Correlation in ITH between SNVs, indels, CNAs and SVs by cancer type.**

977 Evidence of ITH is shown for 1,705 samples with sufficient power to detect subclones
978 above 30% CCF (see **STAR Methods**), as in **Figure 3**. Pairwise scatter plots in the upper
979 triangle show the fractions of subclonal SNVs, indels, CNAs and SVs per tumor sample.
980 Pearson's correlation coefficient, *R*, is separately computed for each panel across all
981 samples. Panels on the diagonal show the kernel density estimate of the distribution of
982 subclonal fractions. In the lower triangle, each point shows the median subclonal fraction
983 per cancer type and intervals indicate the interquartile range. Panels only include samples
984 with at least 5 arm-level CNAs (1,238 / 1,705) and at least 5 SVs (1,609 / 1,705).

985

986 **Figure S4. Summary signature trajectories per cancer type**.

987 The average trajectories for mutation signatures were calculated across tumors of the same
988 cancer type. The color of the line denotes the signature and its width reflects the number
989 of contributing tumors. The trajectories have been centered around the activity at the
990 boundary between clonal and subclonal mutations in order to highlight relative changes in
991 signature activity.

992

993 **Figure S5. Clonality analysis of significantly recurrent breakpoints.**

994 (A) Number and clonality of SVs observed at 52 loci with significantly recurrent
995 breakpoints (SRBs) (Rheinbay et al., 2020). SVs with a subclonal probability larger than
996 50% were considered subclonal and clonal otherwise. (B) Proportion of cancer types
997 contributing to the enrichment of clonal or subclonal SVs in a locus (see **Figure 6A**). The
998 genes on the y-axis represent the most likely driver gene for each locus (Rheinbay et al.,
999 2020).

ACKNOWLEDGMENTS

This work was supported by the Francis Crick Institute, which receives its core funding from Cancer Research UK (FC001202), the UK Medical Research Council (FC001202), and the Wellcome Trust (FC001202). This project was enabled through the Crick Scientific Computing STP and through access to the MRC eMedLab Medical Bioinformatics infrastructure, supported by the Medical Research Council (grant number MR/L016311/1). MT and JD are postdoctoral fellows supported by the European Union's Horizon 2020 research and innovation program (Marie Skłodowska-Curie Grant Agreement No. 747852-SIOMICS and 703594-DECODE). JD is a postdoctoral fellow of the Research Foundation – Flanders (FWO). IVG is supported by a Wellcome Trust PhD fellowship (WT097678) and the Ann and Sol Schreiber Mentored Investigator Award of the Ovarian Cancer Research Alliance. SM is funded by a Vanier Canada Graduate Scholarship. SCS is supported by the NSERC Discovery Frontiers Project, "The Cancer Genome Collaboratory" and by NIH GM108308. DJA is supported by Cancer Research UK. FM, GM and KeY would like to acknowledge the support of the University of Cambridge, Cancer Research UK and Hutchison Whampoa Limited. GM, KeY and FM are funded by CRUK core grants C14303/A17197 and A19274. KeY is further supported by EPSRC EP/R018634/1. SSe and YJ are supported by NIH R01 CA132897. HZ is supported by grant NIMH086633 and an endowed Bao-Shan Jing Professorship in Diagnostic Imaging. PTS is supported by U24CA210957 and 1U24CA143799. WW is supported by the U.S. National Cancer Institute (1R01 CA183793 and P30 CA016672). DCW is funded by the Li Ka Shing foundation. PVL is a Winton Group Leader in recognition of the Winton Charitable Foundation's support towards the establishment of The Francis Crick Institute. We acknowledge the contributions of the many clinical networks across ICGC and TCGA who provided samples and data to the PCAWG Consortium, and the contributions of the Technical Working Group and the Germline Working Group of the PCAWG Consortium for collation, realignment and harmonized variant calling of the cancer genomes used in this study. We thank the patients and their families for their participation in the individual ICGC and TCGA projects. We gratefully acknowledge Nicholas McGranahan and Charles Swanton for valuable comments on our manuscript.

1030 **MEMBERS OF THE PCAWG EVOLUTION AND HETEROGENEITY**
1031 **WORKING GROUP**

1032 Stefan C. Dentro[1,2,3,*], Ignaty Leshchiner[4,*], Moritz Gerstung[5,*], Clemency Jolly[1,*], Kerstin
1033 Haase[1,*], Maxime Tarabichi[1,2,*], Jeff Wintersinger[6,7,*], Amit G. Deshwar[6,7,*], Kaixian Yu[8,*],
1034 Santiago Gonzalez[5,*], Yulia Rubanova[6,7,*], Geoff Macintyre[9,*], Jonas Demeulemeester[1,10,*],
1035 David J. Adams[2], Pavana Anur[11], Rameen Beroukhim[4,12], Paul C. Boutros[6,13], David D.
1036 Bowtell[14], Peter J. Campbell[2], Shaolong Cao[8], Elizabeth L. Christie[14,15], Marek Cmero[15,16],
1037 Yupeng Cun[17], Kevin J. Dawson[2], Nilgun Donmez[18,19], Ruben M. Drews[9], Roland Eils[20,21],
1038 Yu Fan[8], Matthew Fittall[1], Dale W. Garsed[14,15], Gad Getz[4,22,23,24], Gavin Ha[4], Marcin
1039 Imielinski[25,26], Lara Jerman[5,27], Yuan Ji[28,29], Kortine Kleinheinz[20,21], Juhee Lee[30], Henry
1040 Lee-Six[2], Dimitri G. Livitz[4], Salem Malikic[18,19], Florian Markowetz[9], Inigo Martincorena[2],
1041 Thomas J. Mitchell[2,31], Ville Mustonen[32], Layla Oesper[33], Martin Peifer[17], Myron Peto[11],
1042 Benjamin J. Raphael[34], Daniel Rosebrock[4], S. Cenk Sahinalp[19,35], Adriana Salcedo[36],
1043 Matthias Schlesner[20], Steven Schumacher[4], Subhajit Sengupta[28], Ruian Shi[6], Seung Jun
1044 Shin[8,37], Lincoln D. Stein[36], Oliver Spiro[4], Ignacio Vázquez-García[2,31,38,39], Shankar
1045 Vembu[6], David A. Wheeler[40], Tsun-Po Yang[17], Xiaotong Yao[25,26], Ke Yuan[9,41], Hongtu
1046 Zhu[8], Wenyi Wang[8,#], Quaid D. Morris[6,7,#], Paul T. Spellman[11,#], David C. Wedge[3,42,#],
1047 Peter Van Loo[1,#]

1048

1049 [1]The Francis Crick Institute, London NW1 1AT, United Kingdom; [2]Wellcome Trust Sanger
1050 Institute, Cambridge CB10 1SA, United Kingdom; [3]Big Data Institute, University of Oxford,
1051 Oxford OX3 7LF, United Kingdom; [4]Broad Institute of MIT and Harvard, Cambridge, MA 02142,
1052 USA; [5]European Molecular Biology Laboratory, European Bioinformatics Institute, Cambridge
1053 CB10 1SD, United Kingdom; [6]University of Toronto, Toronto, ON M5S 3E1, Canada; [7]Vector
1054 Institute, Toronto, ON M5G 1L7, Canada; [8]The University of Texas MD Anderson Cancer Center,
1055 Houston, TX 77030, USA; [9]Cancer Research UK Cambridge Institute, University of Cambridge,
1056 Cambridge CB2 0RE, United Kingdom; [10]Department of Human Genetics, University of Leuven,
1057 B-3000 Leuven, Belgium; [11]Molecular and Medical Genetics, Oregon Health & Science University,
1058 Portland, OR 97231, USA; [12]Dana-Farber Cancer Institute, Boston, MA 02215, USA; [13]University
1059 of California, Los Angeles, Los Angeles, CA 90095, USA; [14]Peter MacCallum Cancer Centre,
1060 Melbourne, VIC 3000, Australia; [15]University of Melbourne, Melbourne, VIC 3010, Australia;

1061 [16]Walter + Eliza Hall Institute, Melbourne, VIC 3000, Australia; [17]University of Cologne, 50931
1062 Cologne, Germany; [18]Simon Fraser University, Burnaby, BC V5A 1S6, Canada; [19]Vancouver
1063 Prostate Centre, Vancouver, BC V6H 3Z6, Canada; [20]German Cancer Research Center (DKFZ),
1064 69120 Heidelberg, Germany; [21]Heidelberg University, 69120 Heidelberg, Germany;
1065 [22]Massachusetts General Hospital Center for Cancer Research, Charlestown, Massachusetts 02129,
1066 USA; [23]Massachusetts General Hospital, Department of Pathology, Boston, Massachusetts 02114,
1067 USA; [24]Harvard Medical School, Boston, 02215, USA; [25]Weill Cornell Medicine, New York, NY
1068 10065, USA; [26]New York Genome Center, New York, NY 10013, USA; [27]University of Ljubljana,
1069 1000 Ljubljana, Slovenia; [28]NorthShore University HealthSystem, Evanston, IL 60201, USA; [29]The
1070 University of Chicago, Chicago, IL 60637, USA; [30]University of California Santa Cruz, Santa Cruz,
1071 CA 95064, USA; [31]University of Cambridge, Cambridge CB2 0QQ, United Kingdom;
1072 [32]Organismal and Evolutionary Biology Research Programme, Department of Computer Science,
1073 Institute of Biotechnology, University of Helsinki, 00014 Helsinki, Finland; [33]Carleton College,
1074 Northfield, MN 55057, USA; [34]Princeton University, Princeton, NJ 08540, USA; [35]Indiana
1075 University, Bloomington, IN 47405, USA; [36]Ontario Institute for Cancer Research, Toronto, ON
1076 M5G 0A3, Canada; [37]Korea University, Seoul, 02481, Republic of Korea; [38]Computational
1077 Oncology, Memorial Sloan Kettering Cancer Center, New York, NY 10065, USA; [39]Irving Institute
1078 for Cancer Dynamics, Columbia University, New York, NY 10027, USA; [40]Human Genome
1079 Sequencing Center, Baylor College of Medicine, Houston, TX 77030, USA; [41]School of
1080 Computing Science, University of Glasgow, Glasgow G12 8RZ, United Kingdom; [42]Oxford NIHR
1081 Biomedical Research Centre, Oxford OX4 2PG, United Kingdom.

1082 *: These authors contributed equally

1083 [#]: These authors jointly directed the work

Figure 1. Consensus-based characterization of intra-tumor heterogeneity.

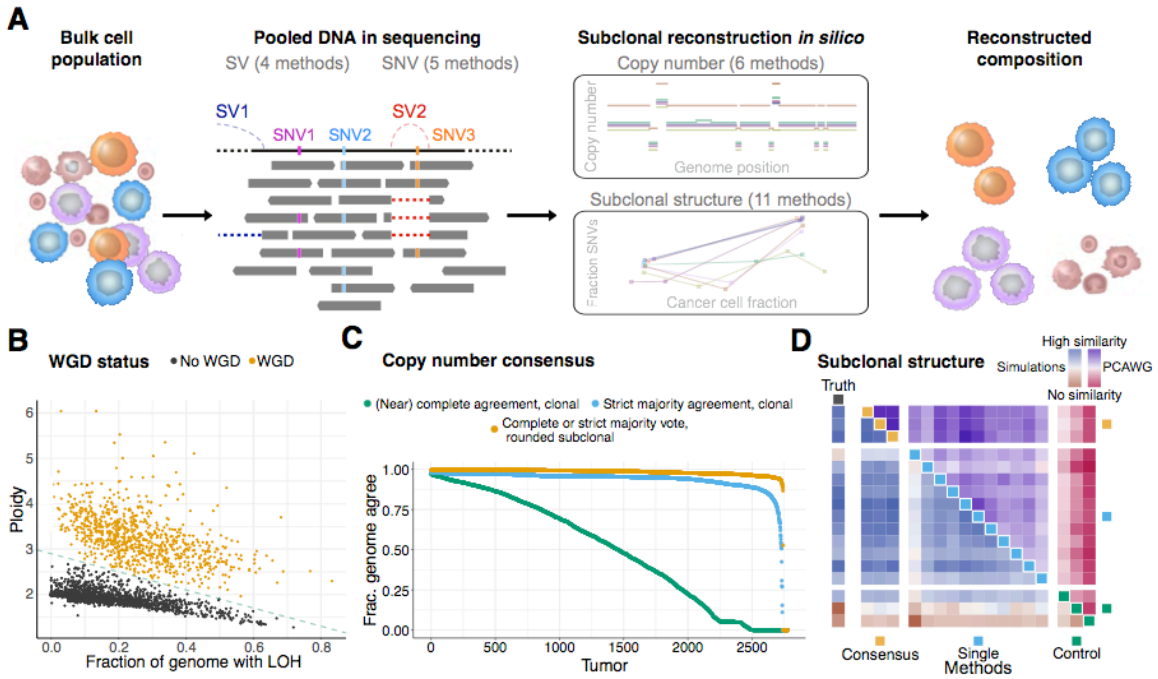

(A) Schematic representation of our consensus-based intra-tumor heterogeneity (ITH) reconstruction from sequencing data. (B) Samples with and without whole-genome duplications separate in two clusters according to their consensus ploidy and the fraction of the genome showing loss of heterozygosity. (C) Agreement between the six copy number callers using a multi-tier consensus copy number calling approach. The three lines denote the fraction of the genome at which agreement is reached at different levels of confidence: (near-)complete agreement on both alleles of clonal copy number, a strict majority agreement on both alleles of clonal copy number and (near-)complete or strict majority agreement on both alleles of rounded subclonal copy number (see **STAR Methods**). At the third level, agreement is reached on an average 93% of the genome. (D) Heatmap of the normalized average pairwise similarities of subclonal architectures identified by 11 individual, 3 consensus, and 3 control reconstruction methods. Each method is represented by one colored square on the diagonal. On rows and columns, each method is compared to all other methods. The upper triangle shows the average pairwise similarities on the 2,778 PCAWG samples, the lower triangle shows the same on a validation set of 965 simulated samples. In the leftmost column similarities are computed against the truth of the simulated set. Color intensities scale with the similarities and were normalized separately for PCAWG, simulations and truth.

Figure 2. Winner's curse correction.

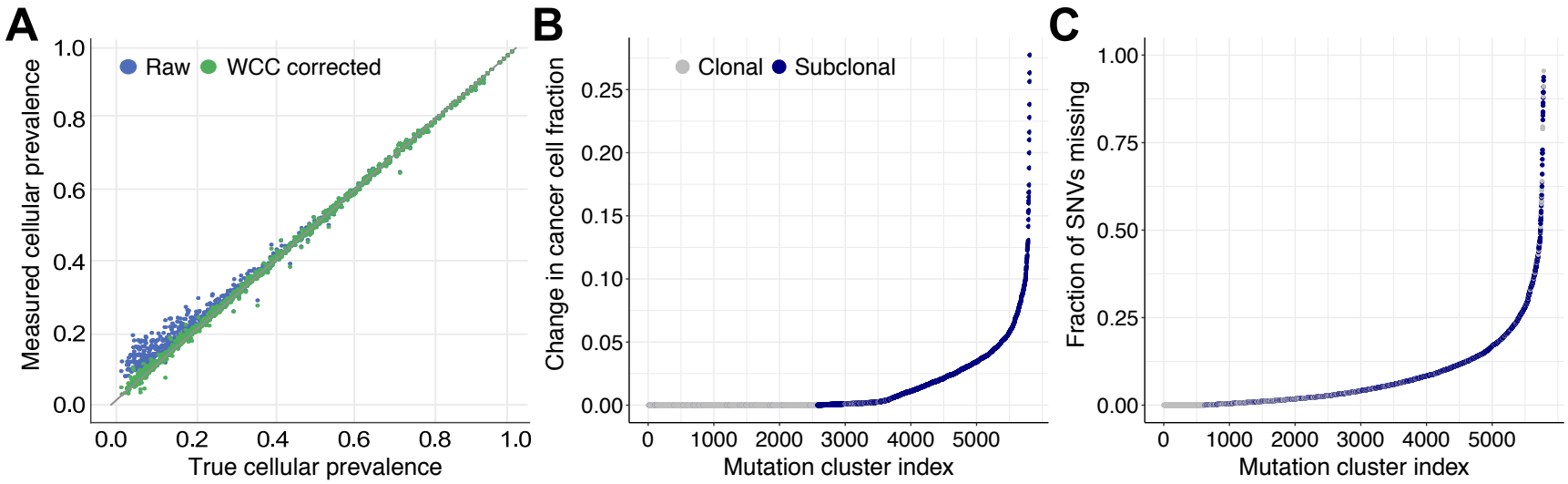

(A) Validation of our approach to adjust for the "winner's curse-like effect, and (B-C) the estimated cluster-CCF and mutation adjustment in all mutation clusters identified in the study. Subclonal clusters show a shift to larger CCF values after correction (B) and the majority of clusters are estimated to contain additional missed SNVs (C).

Figure 3. Overview and characterization of ITH across cancer types.

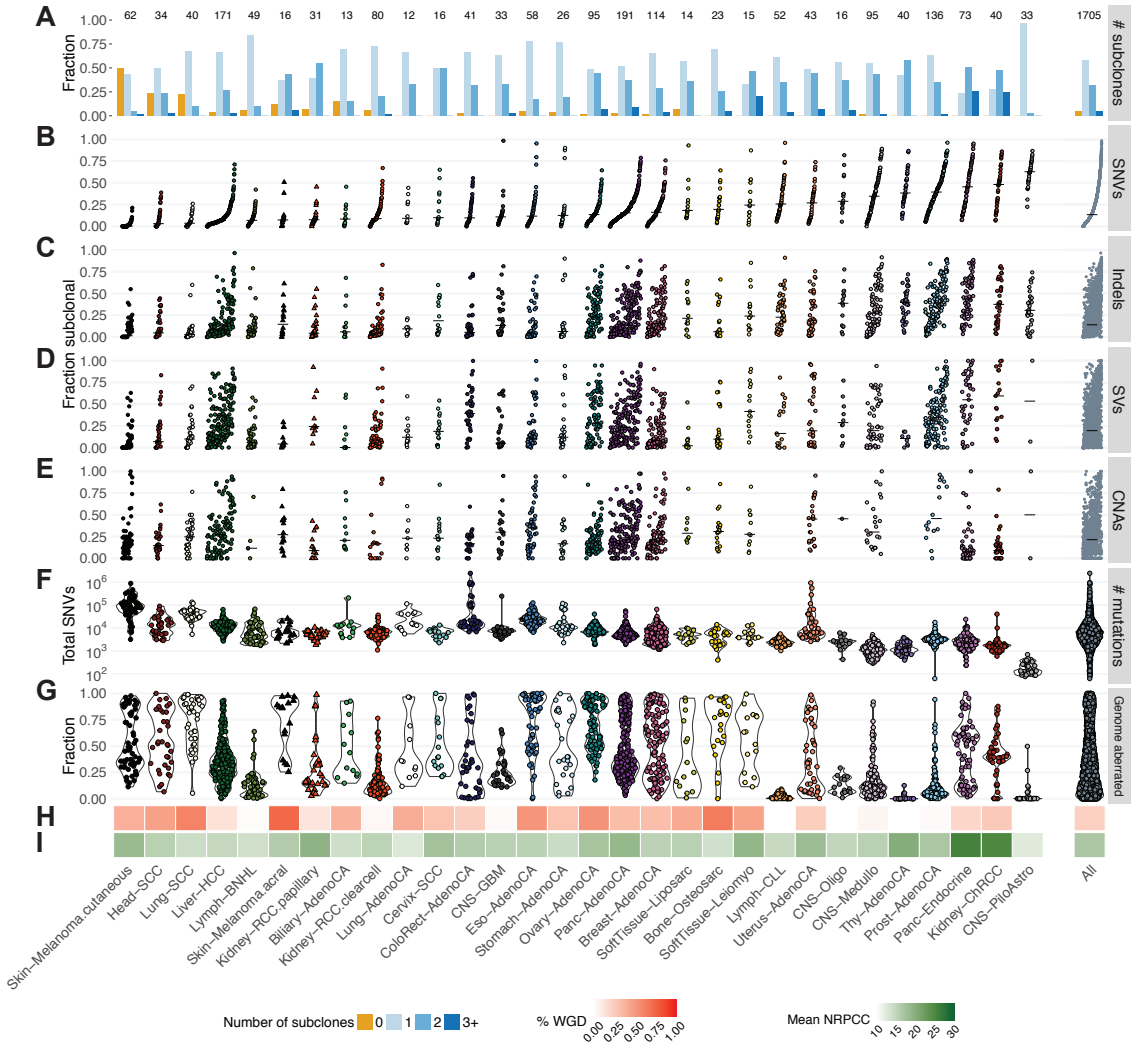

Evidence of ITH is shown for 1,705 samples with sufficient power to detect subclones at CCF > 30% (see **STAR Methods**). Samples have been limited to those with less than 2% tumor contamination in the matched normal sample and no activity of any of the identified artefact signatures (Alexandrov et al., 2020). Only representative samples (The ICGC/TCGA Pan-Cancer Analysis of Whole Genomes Consortium, 2020) from multi-sample cases are shown. (A) Bar plot showing the fraction of samples with given number of subclones; (B-E) Scatter plots showing the fractions of subclonal SNVs, indels, SVs and subclonal arm-level CNAs (the latter two mutation types are only plotted for samples that have at least 5 events, sample order is determined by increasing fraction of subclonal SNVs and conserved in the other three panels); Violin plots showing the total mutation burden (F) and overall fraction of the genome that does not have a copy number state of 1+1, or 2+2 in WGD samples (G); Heatmaps showing the fraction of tumor samples with whole genome duplications (H) and the mean power to identify subclones per cancer types (number of reads per clonal copy – nrpcc, see **STAR Methods)** (I)**.**

Figure 4. Further characterization of ITH using mutation phasing.

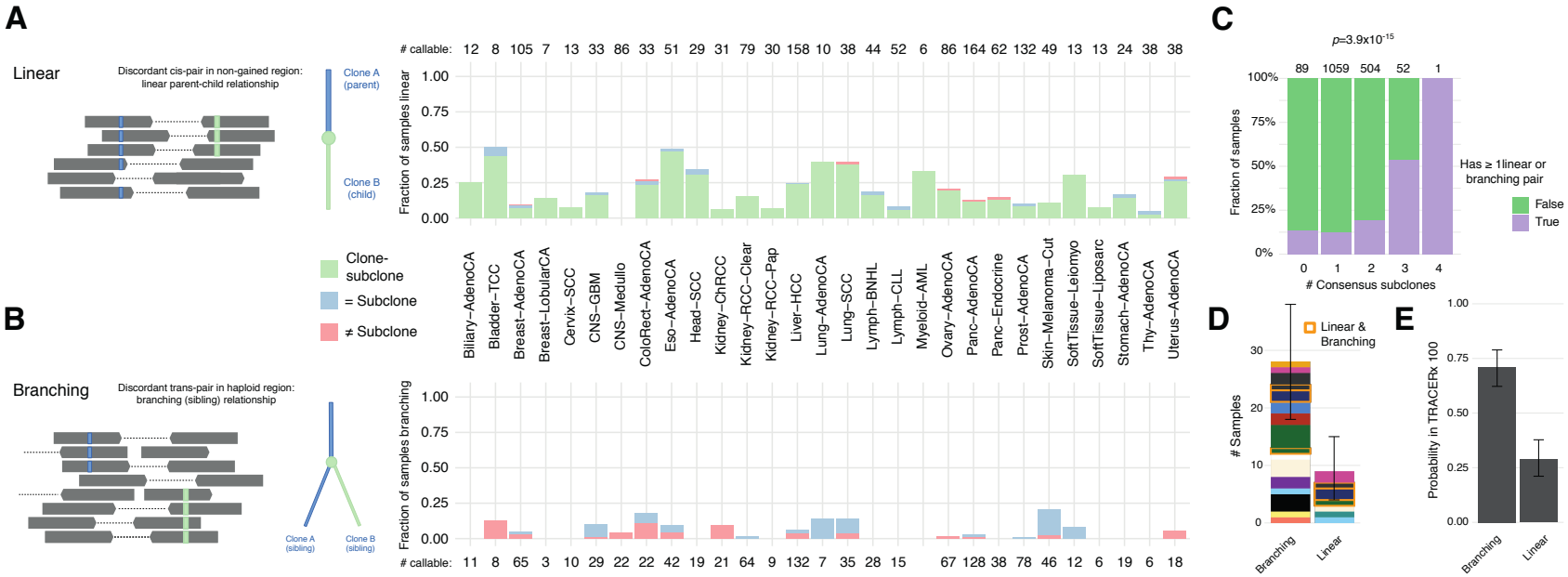

(A-B) Proportion of powered tumors with evidence of linear and branching phylogenies, through analysis of phased reads of variants in-*cis* (A) or in-*trans* (B) among tumors with at least one phaseable pair in the appropriate context. (C) Fraction of powered samples, stratified by number of consensus subclones, with at least one linear or branching pair (χ^2-test for independence). (D) Number of samples with linear or branching pairs when sets are filtered to be comparable. Error bars indicate the 95% bootstrap interval. Samples are colored by tumor type and boxed (orange) when they present with pairs of both types. (E) Probabilities of observing a linear *vs.* branching relationship when picking two random subclones from TRACERx 100 trees (Jamal-Hanjani et al., 2017). Error bars indicate the 95% bootstrap interval.

Figure 5. Subclonal boundaries are associated with changes in mutation signature activity.

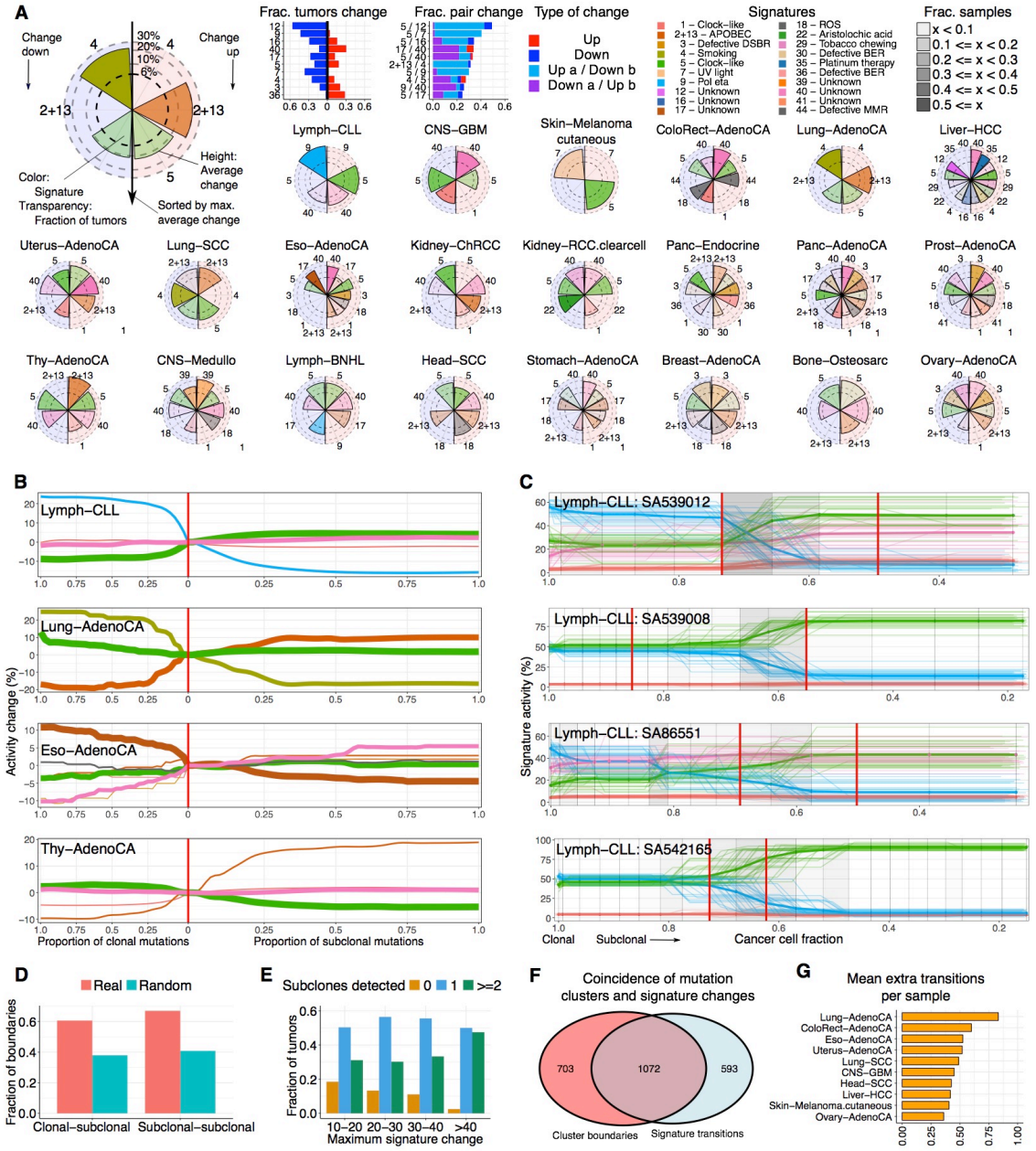

(A) Mutation signature changes across cancer types. Bar graphs show the proportion of tumors in which signature (pairs) change and radial plots provide a view per cancer type. Each radial plot contains the signatures that are active in at least 5 tumors and change (≥ 6%) in at least 3 tumors. The left and right side of the radial plot represent signatures that become less and more active, respectively. The height of a wedge represents the average activity change (log scale), the color denotes the signature and the transparency shows the fraction of tumors in which the signature changes (as a proportion of the tumors in which the signature is active). Signatures are sorted around the radial plot (top-to-bottom) by

maximum average activity change. (B) Average signature trajectories for selected cancer types. Each line is colored by signature and corresponds to the average activity across tumors of this cancer type in which the signature is active. The width of the line represents the number of tumors that are represented. Mutations are split into clonal and subclonal, visually divided by a red vertical line. (C) Signature trajectories for selected individual CLL tumors. Each line corresponds to an activity trajectory derived from a bootstrap sample of SNVs. The grey vertical grid represents the mutation bins. These are colored grey when a significant change in signature activity is detected. Red vertical lines represent consensus subclonal mutation clusters. (D) The fraction of signature change points that coincide with boundaries between mutation clusters, as compared to what is expected when randomly placing change points. (E) The number of subclones detected in tumors grouped by the maximum detected signature activity change. (F) An overview of coinciding SNV cluster boundaries and signature activity change points. (G) The average number of additional signature change points detected per tumor.

Figure 6. Driver mutations and subclonal selection.

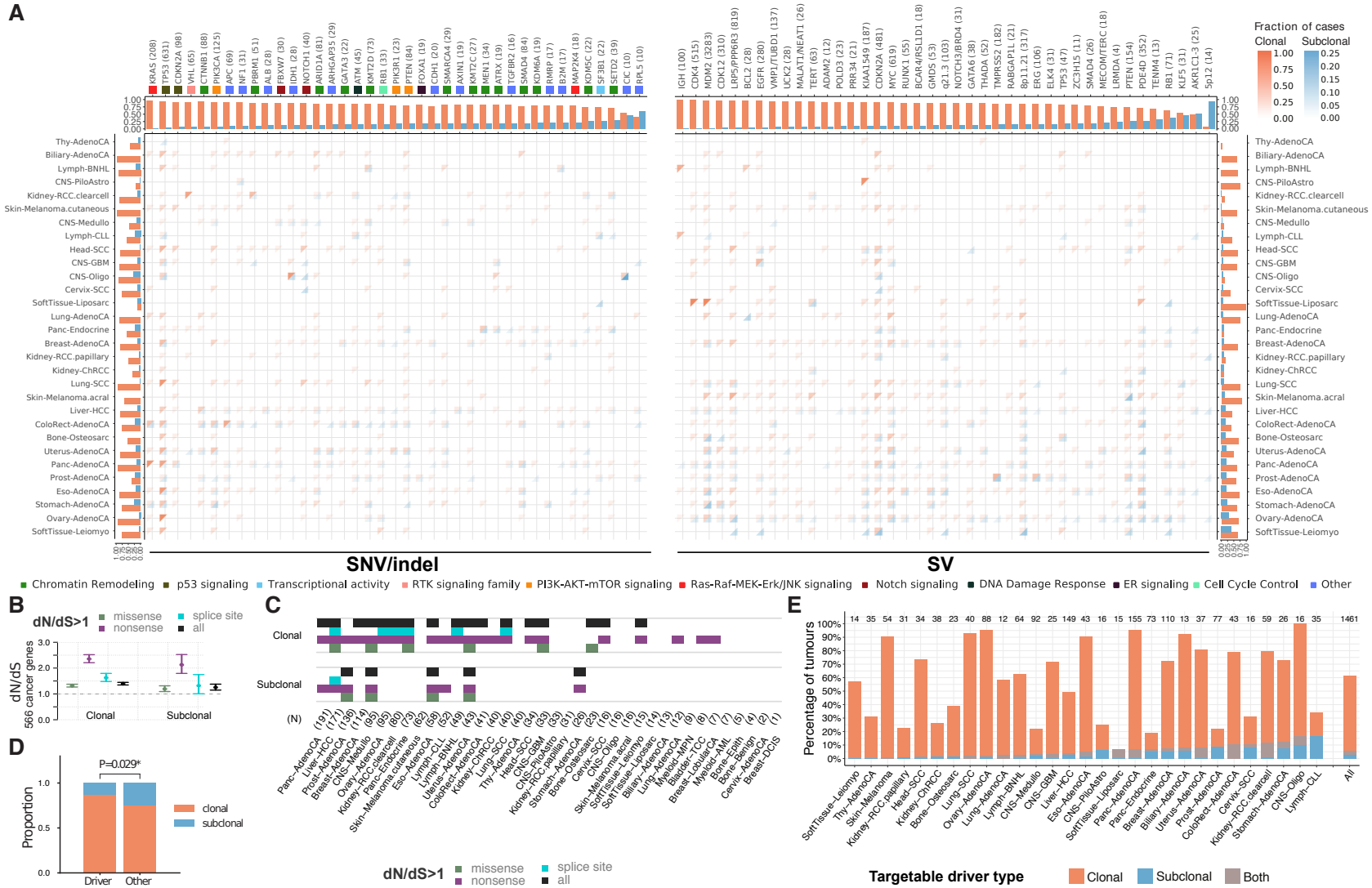

(A) Heatmap of the fraction of samples of the different cancer types with clonal (orange) and subclonal (blue) driver substitutions and indels (left panel) and structural variants (right panel). Marginal bar plots represent the fraction of clonal and subclonal driver mutations in each cancer type (side) and each driver gene or candidate region (top). Only genes with at least 4 subclonal driver mutations are shown. For SNVs and indel drivers (top left panel), gene set and pathway annotations highlight an enrichment of subclonally mutated drivers in chromatin remodeling. (B) dN/dS values for clonal and subclonal SNVs in 566 established cancer genes across all primary tumors. Values for missense, nonsense, splice site, and all mutations are shown, along with the 95% confidence intervals. (C) Cancer and mutation types for which dN/dS is significantly greater than 1 (95% confidence intervals>1) for clonal and subclonal mutations. Cancer types are ordered by the total number of samples. (D) Proportions of (sub)clonal driver gene fusions versus non-driver fusions. (E) Survey of targetable driver mutations across cancer types, stratified by clonal status.

Figure S1. Validation of consensus purity values.

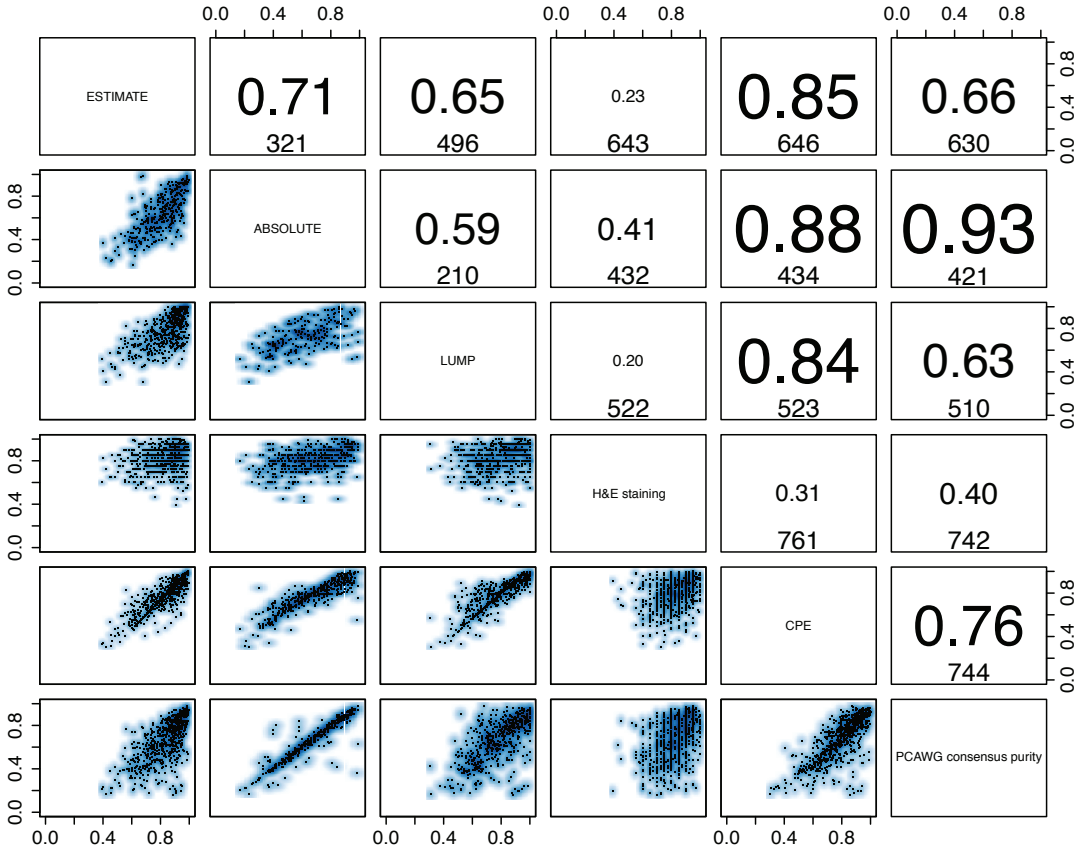

The lower triangle shows pairwise scatterplots of the purities obtained through expression profiles of a panel of immune and stromal genes (ESTIMATE), somatic copy number data (ABSOLUTE), leukocyte unmethylation (LUMP), image analysis by hematoxylin and eosin staining (H&E staining), and consensus purity as derived by Aran *et al*. (Aran et al., 2015) (CPE). The top triangle shows the respective Pearson correlation coefficients and the number of samples that have both purity estimates available.

Figure S2. Power analysis of the consensus subclonal architecture approach.

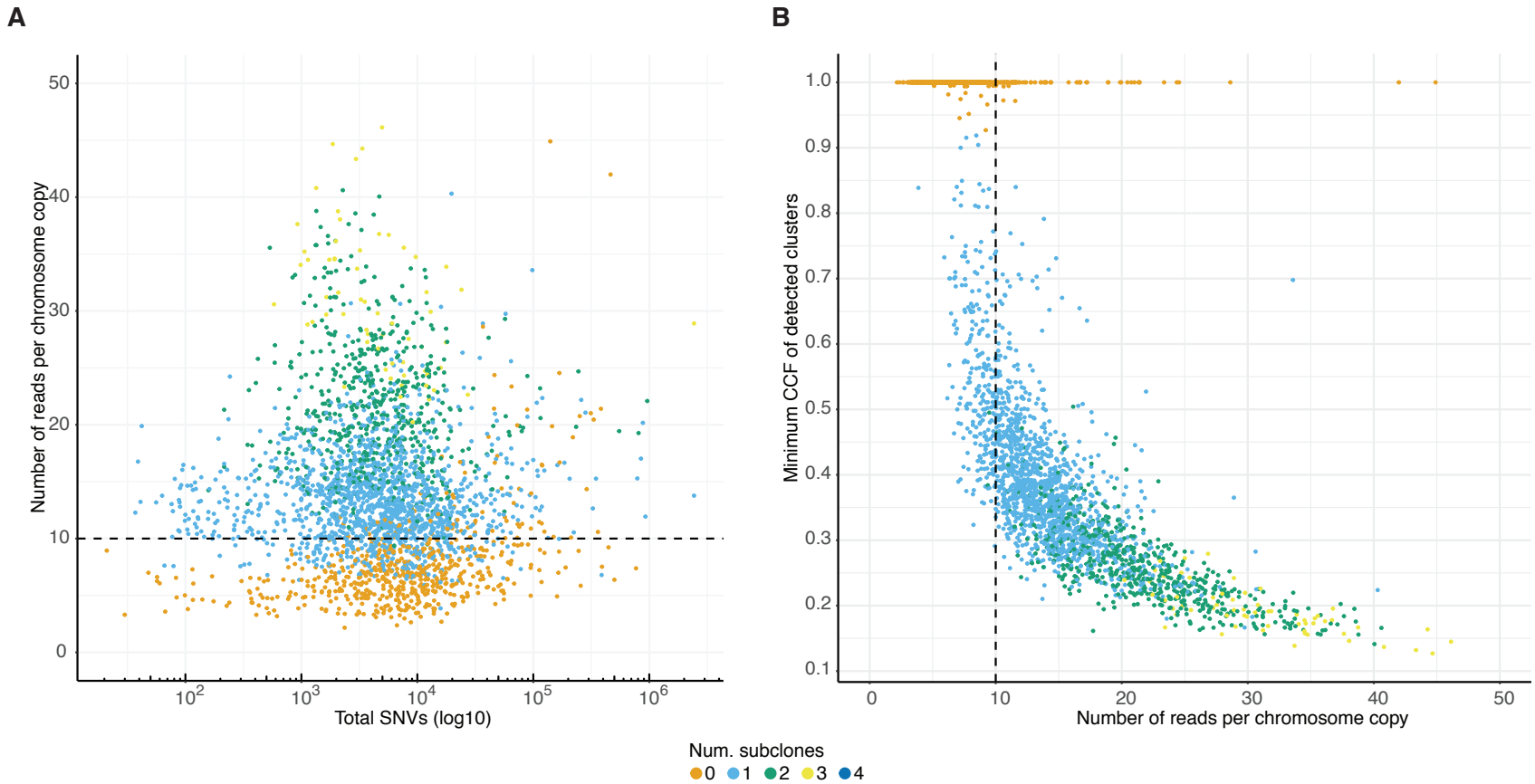

(A) Our ability to detect subclones depends, not on the number of detected SNVs, but on the number of reads per clonal copy (nrpcc) available. This metric takes tumor purity, ploidy and sequencing coverage into account (see **STAR Methods**). We control for this effect by including only tumors with nrpcc ≥ 10. In these tumors, we should be sufficiently powered to detect a subclone at a CCF as low as 30% (see **STAR Methods**). This becomes clear from (B) which shows the minimum CCF of the detected clusters in each tumor against the number of reads per chromosome copy.

Figure S3. Correlation in ITH between SNVs, indels, CNAs and SVs by cancer type.

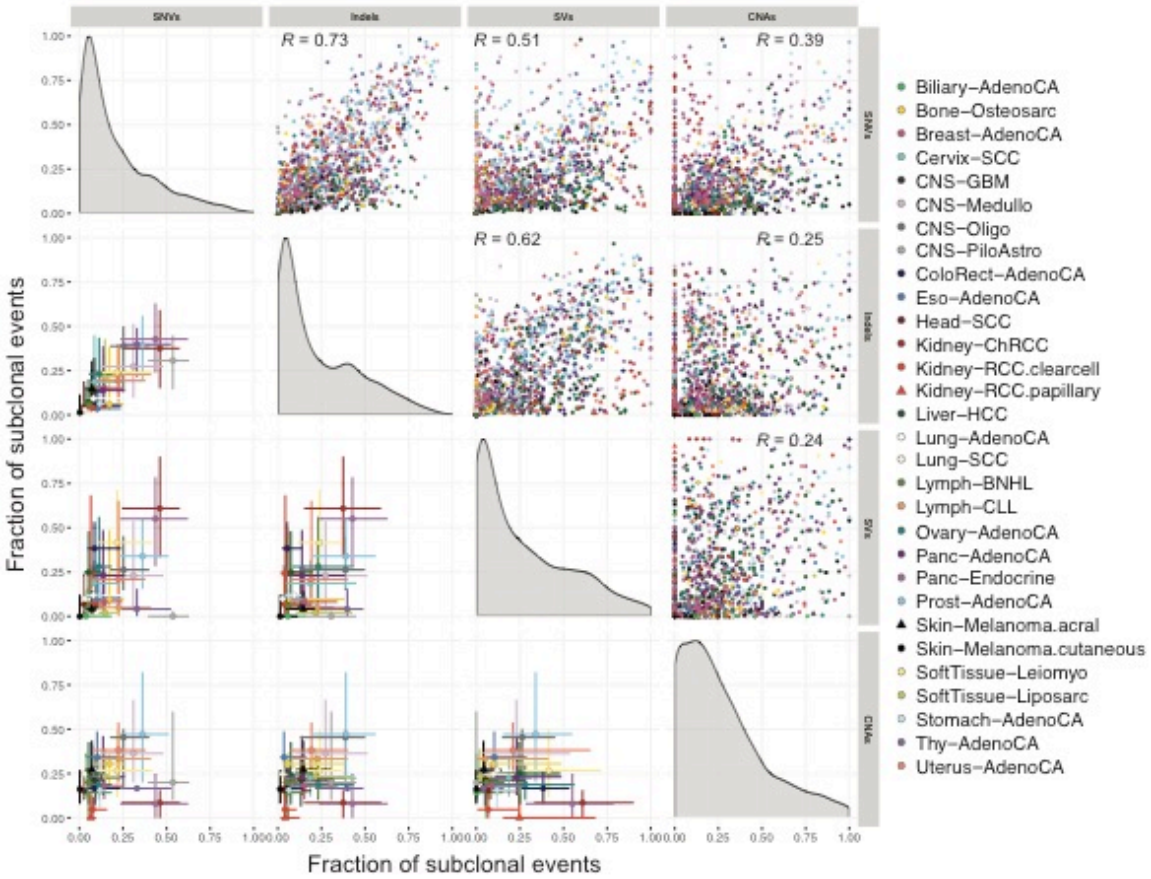

Evidence of ITH is shown for 1,705 samples with sufficient power to detect subclones above 30% CCF (see **STAR Methods**), as in **Figure 3**. Pairwise scatter plots in the upper triangle show the fractions of subclonal SNVs, indels, CNAs and SVs per tumor sample. Pearson's correlation coefficient, *R*, is separately computed for each panel across all samples. Panels on the diagonal show the kernel density estimate of the distribution of subclonal fractions. In the lower triangle, each point shows the median subclonal fraction per cancer type and intervals indicate the interquartile range. Panels only include samples with at least 5 arm-level CNAs (1,238 / 1,705) and at least 5 SVs (1,609 / 1,705).

Figure S4. Summary signature trajectories per cancer type.

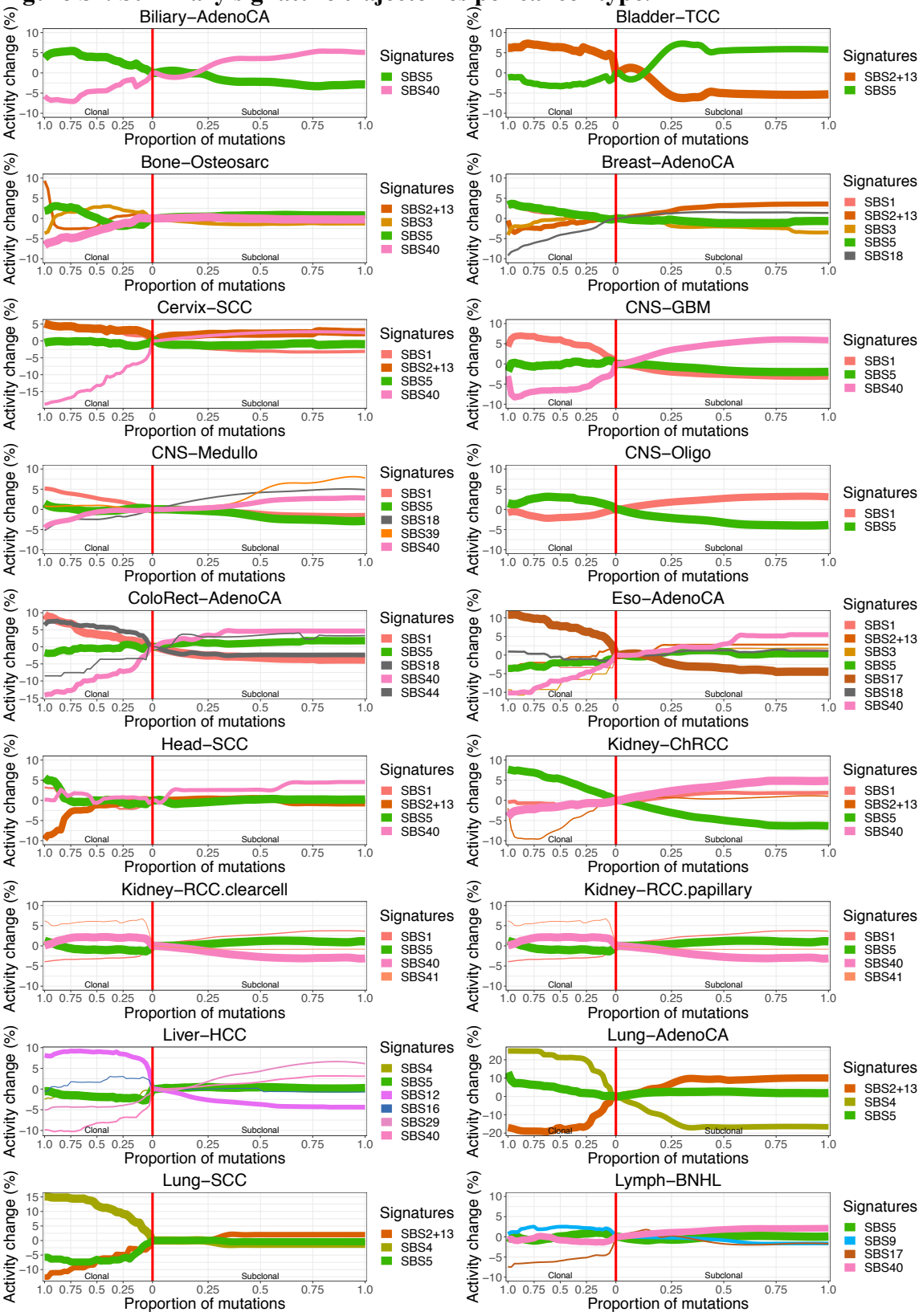

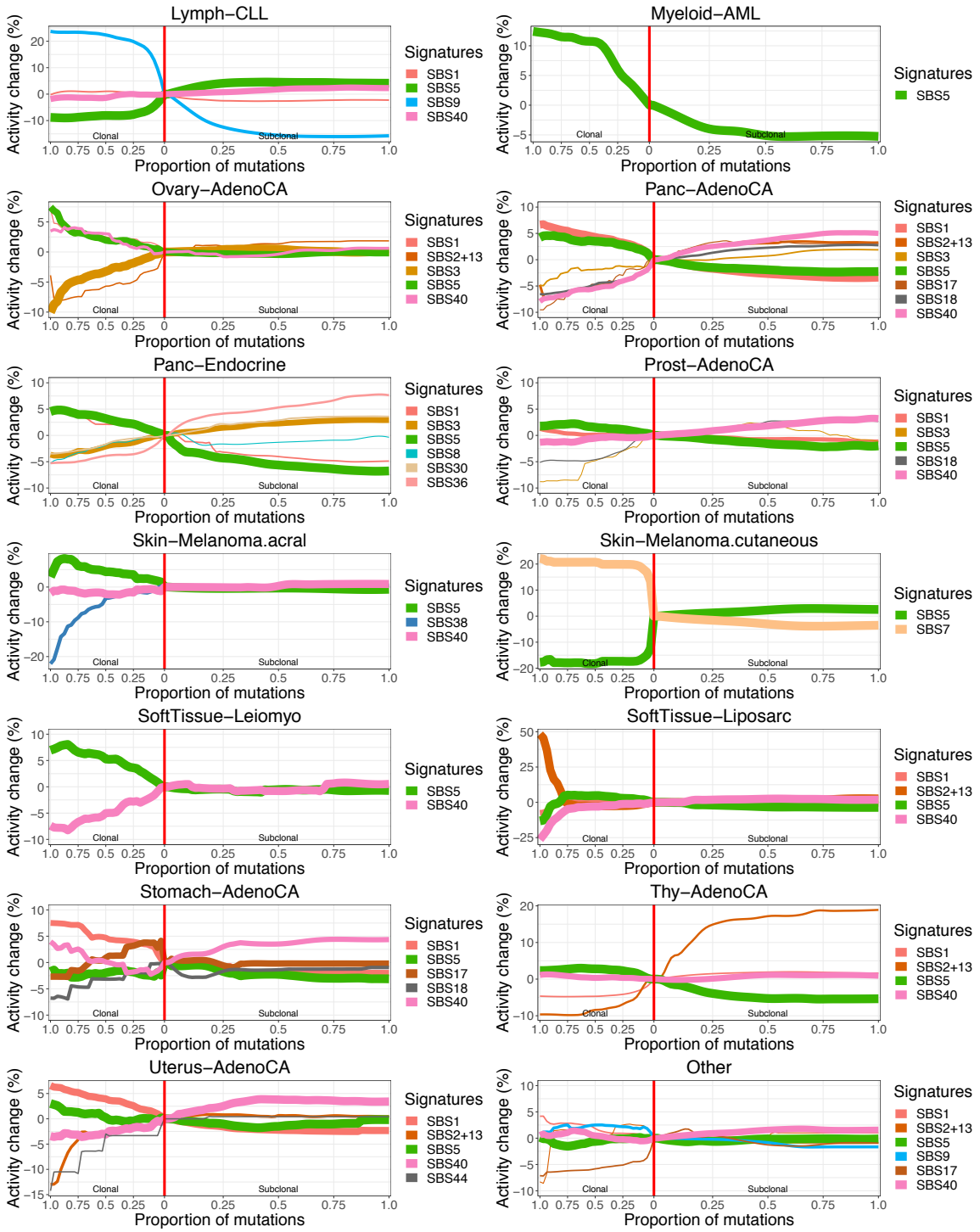

The average trajectories for mutation signatures were calculated across tumors of the same cancer type. The color of the line denotes the signature and its width reflects the number of contributing tumors. The trajectories have been centered around the activity at the boundary between clonal and subclonal mutations in order to highlight relative changes in signature activity.

Figure S5. Clonality analysis of significantly recurrent breakpoints.

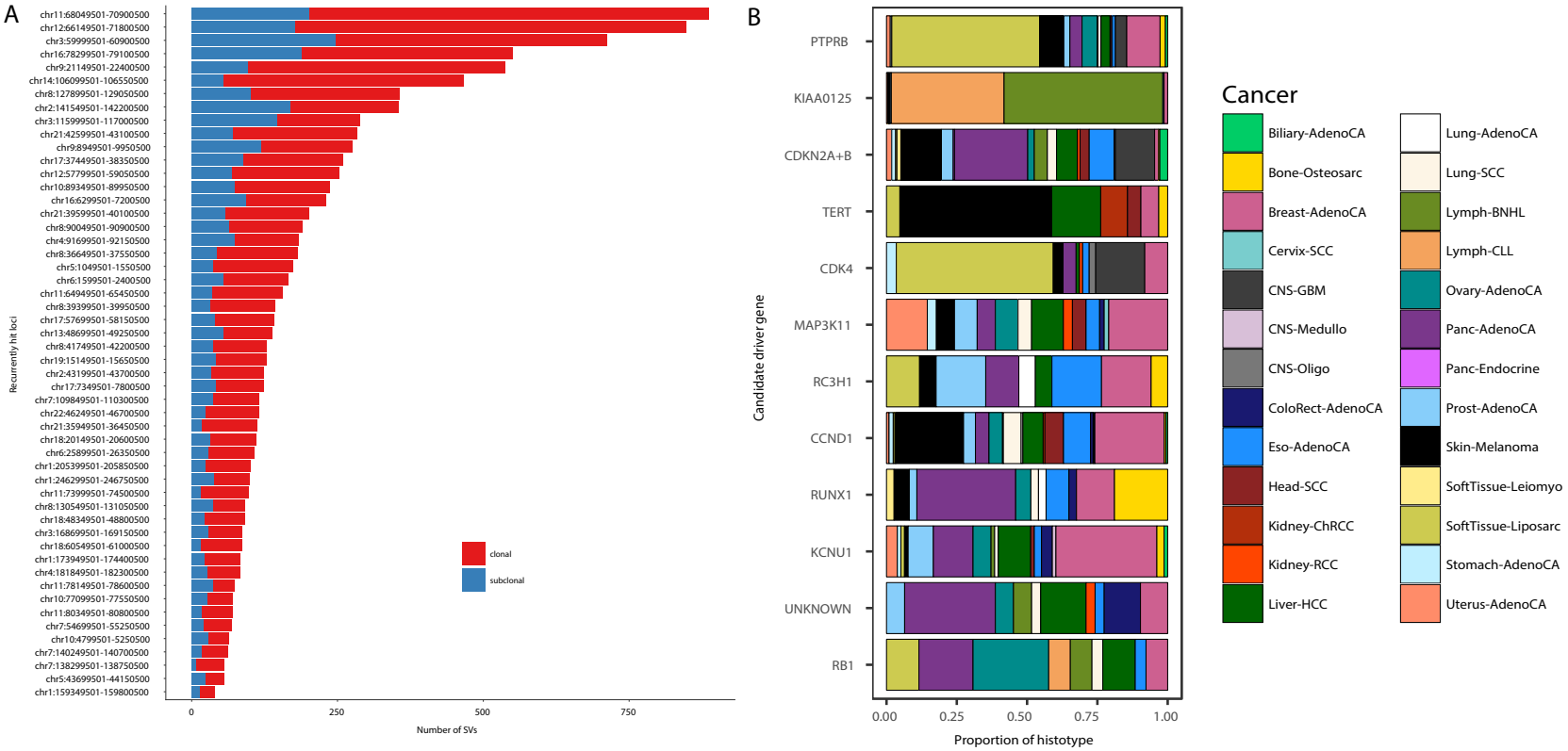

(A) Number and clonality of SVs observed at 52 loci with significantly recurrent breakpoints (SRBs) (Rheinbay et al., 2020). SVs with a subclonal probability larger than 50% were considered subclonal and clonal otherwise. (B) Proportion of cancer types contributing to the enrichment of clonal or subclonal SVs in a locus (see **Figure 6A**). The genes on the y-axis represent the most likely driver gene for each locus (Rheinbay et al., 2020).